university of groningen / faculty of science and engineering

July 2022

Kinematics of Very Metal-Poor Stars in the Inner Regions of Aurigaia Galaxies

Abstract

The bulge in the Milky Way is known to be a Boxy/Peanut bulge, however recent observations show that a spherical, non-rotating component might be hiding in the metal-poor populations. These observations show that the strength of the rotational signal decreases with metallicity, to almost no rotation for very metal-poor stars ($[\mathrm{Fe/H}] < -2$). In this thesis we reproduce the-pattern using a Gaia DR2 mock of a subset of the AURIGA cosmological magneto-hydrodynamical simulated galaxies, showing that the rotational fall-off is not unique to the Milky Way. Moreover, we show that observations of this pattern are roboust against a range of selection effects, and therefore are representative of what most likely is the underlying reality. Finally, we look at a connection with the merger history of the galaxies, qualitatively showing that bulge rotation decreases in galaxies with an active merger history until populations with metallicity $-1 < [\mathrm{Fe/H}] < -0.5$, or ages between $8 - 9\,\mathrm{Gyr}$. For galaxies with a more quiescent merger history, the decrease in rotation continues until metallicities $-1.5 < [\mathrm{Fe/H}] < -1$ (or ages $> 12\,\mathrm{Gyr}$). The latter results suggest that by measuring rotational fall-off, we can put constraints on major merger events in the Milky Way.

Astronomy Bachelor's Thesis

Author: Sten Sipma

Primary supervisor: Else Starkenburg

Contents

1 Introduction

The inner regions of the Milky Way (MW) can tell us a lot about the dynamics of our galaxy, which makes it an interesting region to study. In the MW we can resolve individual stars, but this is not the case for other galaxies. We can therefore apply the knowledge gained from studying MW dynamics to other galaxies. Our position in the MW, however, poses a lot of observational challenges due all the intermediate disk material in the form of stars, gas and dust. We therefore either have to observe within non-visual wavelength regimes (like infrared Babusiaux & Gilmore, 2005) or observe at regions of higher galactic latitude (like Ness et al., 2013; Kunder et al., 2012; Arentsen et al., 2020b, at $|b| > 4°$). In addition to physical observations, we can make simulations of galaxies (like Grand et al., 2017; Shen et al., 2010) and compare their results with observations. Finally, we are not restricted to the MW and can learn a lot from observing and classifying other galaxies. Although this does not necessarily bring the same details, it allows us to put the MW in a broader perspective.

1.1 The Milky Way Bulge

It is well established that the MW is a spiral galaxy with a thick and thin disk containing spiral arms, a bulge in the center and a large spherical halo surrounding the disk (Sparke & Gallagher III, 2007). Most spiral galaxies seem to have bulges which can be subdivided into two categories; a Classical Bulge (ClB) and a Pseudobulge (PsB) (Fisher & Drory, 2016; Barbuy et al., 2018). Classical Bulges have properties similar to elliptical galaxies, with mainly pressure supported kinematics, spheroidal rotation, round isophotes and high anisotropy ($v_r/\sigma_r < 1$)[1] (Kormendy & Illingworth, 1982). The typical Sérsic index for a ClB is $n > 2$, again similar to ellipticals. Pseudobulges often have a more disk-like appearance and includes Boxy/Peanut (B/P) and Disky bulges. They typically are rotationally supported with cylindrical rotation ($v_r/\sigma_r \geq 1$), have flat isophotes, flat dispersion profiles and their Sérsic index ($n < 2$) gives a more exponential surface brightness profile. ClBs are mostly found in early type spirals and none are found in type Sc or later. PsBs are found across all spiral types. Some galaxies also seem to have a combination of both a ClB and a PsB (Erwin et al., 2015). Evidence for a (barred) B/P bulge in our MW comes from star counts at higher latitudes, revealing an X-shaped component (McWilliam & Zoccali, 2010), which is shown to be a manifestation of a B/P bulge (Wegg & Gerhard, 2013). The MW also shows cylindrical rotation, consistent with a B/P bulge. The velocity dispersions measured in the central regions of the bulge were around $\sigma \approx 140\mathrm{km\,s^{-1}}$, which lies between typical values of PsBs ($70 - 150\mathrm{km\,s^{-1}}$) and ClBs ($100 - 230\mathrm{km\,s^{-1}}$) (Barbuy et al., 2018).

The colour-magnitude diagram (CMD) analysis of bulge stars has shown that the bulge is largely dominated by an old population ($\sim$ 11 Gyr), having solar metallicities ([Fe/H] $\sim$ 0.0 ± 0.4) (Clarkson et al., 2008). The presence of young stars in the bulge is still a point of dicussion, where CMDs seem to show no evidence of stars around ages $5 - 10$ Gyr (Gennaro et al., 2014), but more recent observations of microlensed dwarfs indicate that stars do exist that are younger than 9 Gyr (Bensby, T. et al., 2017). Older populations are also present in the bulge, and are an important factor for studying the early phases of bulge formation, as it is believed the earliest stars could have formed just 550Myr after the Big Bang (Planck Collaboration et al., 2016). Simulations have shown that these very old and metal-poor stars mainly reside in the inner regions of galaxies (Diemand et al., 2005; Tumlinson, 2010; Starkenburg et al., 2017a), making this an important region of the galaxy to study them.

A commonly studied old population of stars are the variable RR Lyrae stars (RRLs), which peak in their metallicity distribution around [Fe/H] = 1.0. Studying these variable stars is convenient, as they are well known standard candles and therefore their position can be accurately determined (Kunder, 2022). The kinematics and distribution of these RRLs appear to be more consistent with a ClB, contrary to the B/P shape of the general bulge population (Kunder et al., 2012). Simulations have put constraints on the size of a potential ClB, stating that at least 90% of the stars are part of the B/P bulge (Shen et al., 2010). An alternative explanation for the RRL observations, which has not yet been ruled out, is that these high dispersion stars are part of the halo component and are merely passing through the bulge. However, Kunder et al. (2016) observed these RRLs close to the galactic plane, where the surface density is usually dominated by bulge stars, wich would favour the theory of a metal-poor ClB, but not rule out interlopers.

1.2 Rotation in the Metal-Poor Components

Surveys have also looked for stars that are even older than the typical RRLs, specifically for very metal-poor stars ([Fe/H] < -2.0), however only a very small sample of stars have been identified (only 50 as of the writing of Barbuy et al. (2018)). Since then, the Pristine survey (Starkenburg et al., 2017b) has been set up to look for extremely metal-poor stars in the MW halo, reaching metallicities of [Fe/H] < -4.0. Pristine uses a

[1] v_r and σ_r are the radial (or line of sight) velocity and -dispersions respectively.

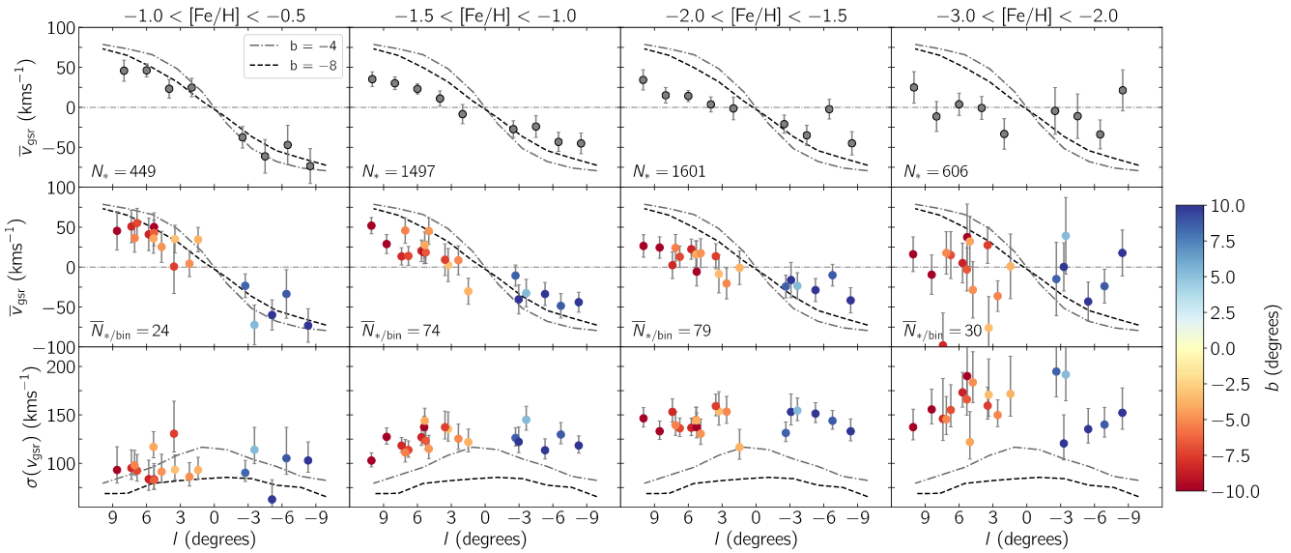

Figure 1: Results from Arentsen et al. (2020a), showing a decrease in rotation (and increase in dispersion) in the galactic plane, for a decrease in metallicity. Top row: longitude versus mean line-of-sight velocity in the GSR ($v_{\rm gsr}$) for different metallicity ranges from left to right (see column title) in bins of 2°. This includes both the normal giants and the HB stars. Lines from the bar model from Shen et al. (2010) have been overplotted. Error bars are $\sigma/\sqrt{N}$. Middle row: the same, but separately for each AAT (Anglo-Australian Telescope) field where the colour indicates the latitude. Bottom row: similar, but for the standard deviation of $v_{\rm gsr}$. In each of the panels, only bins with at least 10 stars are shown. The (asymmetric) error bars are $\sqrt{\sigma^2(N-1)\chi^2_{\pm}}$, with $\chi_{\pm}$ determined for a 68 per cent confidence interval and $N-1$ degrees of freedom.

narrow-band filter for the Ca H and K lines (the *CaHK* filter hereafter) on the Canada-French-Hawaii Telescope (CFHT), in combination with broad-band photometry (the Sloan Digital Sky Survey (SDSS) (York et al., 2000) for Starkenburg et al. (2017b)) to find stellar metallicities. Such a photometric approach is able to derive metallicities for roughly all stars in the field-of-view of the telescope, and therefore can gather significantly more data than a spectroscope. A subset of this survey, focused on stars in the inner MW, is the Pristine Inner Galactic Survey (PIGS) by Arentsen et al. (2020b). Instead of SDSS, the data from Gaia data release 2 (DR2) (Gaia Collaboration et al., 2018), and later Pan-STARRS1 DR1 (Chambers et al., 2016), have been used for the broad-band photometry. The photometric metallicities are then used to select stars for spectroscopic follow up by the AAOmega + 2dF multifibre spectrograph on the 3.9-m Anglo-Australian Telescope (AAT).

PIGS reveals a sample of 1300 very metal-poor stars in the bulge, which is significantly larger than earlier attempts. The kinematics of these PIGS stars have been presented in Arentsen et al. (2020a) and can also be seen in Figures 1 and 2. The first figure compares the observed mean radial velocities (with respect to the galactic standard of rest (GSR)) and the velocity dispersions (i.e. standard deviation of the radial velocities) as a function of galactic latitude l. Moreover, they look at this relation in bins of decreasing metallicity: [Fe/H] : $[-1.0, -0.5], [-1.0, -1.5], [-1.5, -2.0], [-2.0, -3.0]$. Compared to the general MW model by Shen et al. (2010), we see that there is disagreement between the model and lower metallicity populations. In the left columns of the first row in Figure 1, we see that the stars still show strong signs of rotation, but this rotation slows down and finally disappears as we go towards lower metallicity populations. The second row of the figure shows the same trend, but now with individual datapoints corresponding to stars in the same observational field. The final row shows the velocity dispersions compared to the same Shen et al. (2010) model, where we see that the dispersions increase as metallicity decreases. Figure 2 shows the velocity dispersions combined over the entire longitude range in smaller metallicity bins. This again shows that the velocity dispersion increases with decreasing metallicity, agreeing with the RRL dispersions from Kunder et al. (2016), which are also included in the figure.

The flattening in the rotation observed by Arentsen et al. (2020a) has also been seen in simulated galaxies with B/P bulges, like those of AURIGA (Grand et al., 2017, and Section 2.1), where Fragkoudi et al. (2020) looked at the radial velocities and velocity dispersions (in GSR) at latitudes $|b| < 1°$. In all of these bulges, a decrease in the rotation was found towards the metal poor bins ($[0, -0.5], [-0.5, -1]$ and [Fe/H] > -1, but no extra detail in [Fe/H] > -1), but the degree of flattening was found to differ between the bulges. They found that the galaxies which showed a larger decrease in rotation, also had relatively strong or recent merger events. When such a merger occurs after an in-situ population has already formed it would be disrupted and therefore show more anisotropy in the velocity patterns. Younger populations born after the merger will not be disrupted

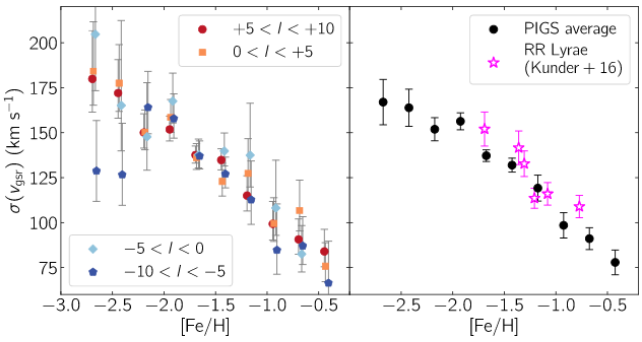

Figure 2: Results from Arentsen et al. (2020a) showing the increase in velocity dispersion with decrease in metallicity [Fe/H] . Left: $v_{\rm gsr}$ dispersion as a function of [Fe/H] (bins of 0.25dex), for four ranges in l. The HB stars are excluded. Different l ranges are offset by 0.01dex for clarity. Only bins with at least 10 stars are shown. Right: weighted average of the different l ranges, with the bulge RR Lyrae results from Kunder et al. (2016).

and go on to form a strong bar. Fragkoudi et al. (2020) concludes that because the galaxies with a quiescent merger history follow a MW-like decrease in rotation, the MW should similarly have a quiet merger history.

1.3 Thesis Overview

In this thesis we will follow up on the results of Arentsen et al. (2020a) and look the kinematics of spiral galaxy bulges in the magneto-hydrodynamical (MHD) AURIGA simulations (Grand et al., 2017) similar to Fragkoudi et al. (2020). We will, however, be taking a more observational approach by using the DR2 mocks of AURIGA: Aurigaia (Grand et al., 2018). This allows us to quantify the possible effects of the observing strategy that, in order to avoid the most extincted areas for the blue CaHK filter, looks much more above the plane of the Galaxy than regarded in the Fragkoudi et al. (2020) study. Additionally, we can investigate the role of other possible selection effects in the observations and we have a closer look at the more metal-poor bins.

We will start by reproducing the results of Arentsen et al. (2020a) by making similar selections on a MW analogue in Aurigaia. Then we will see what the effect is of observational uncertainties and selections on the observed kinematics. After which, we also look at the the other mocked Aurigaia galaxies, which have different properties from the MW analogue. Finally, we will look more into possible causes of the decreasing rotation, such as the connection to mergers and differences between in-situ and accreted stars.

In the following section (Section 2), we will give an introduction to the AURIGA MHD simulation, the Aurigaia DR2 mocks and present the steps we take in order to perform our analysis. We then present our results in Section 3, and follow it by a discussion in Section 4. Finally, we summarise the thesis by presenting our conclusions in Section 5.

2 Methods

In this section, we will give an overview of our methods and introduce the tools which we used for our analysis. We will be using Aurigaia (Grand et al., 2018), a DR2 mock catalogue of a subset of the AURIGA cosmological MHD simulations by Grand et al. (2017). We will introduce the simulations and mocks in the following two subsections. Then, we describe the steps taken in order to use the Aurigaia mocks for our analysis. The final subsection will outline our analysis, of which the results are presented in Section 3.

2.1 AURIGA

AURIGA (Grand et al., 2017) is a set of 30 cosmological MHD zoom simulations of galaxies with MW mass halos. The simulations combine the moving mesh code AREPO (Springel, 2010) with a model for galaxy formation that includes, among others, active galactic nuclei (AGN) feedback, stellar feedback and magnetic fields. AURIGA's main goals are to simulate the formation and evolution of MW sized late-type galaxies, on a resolution level where the characteristic patterns of late-type galaxies (like bars and spiral arms) are resolvable. The 30 simulations allow for a quantitative comparison of galaxy formation history, like disk growth and merger history. The following describe AURIGA in reasonable depth, however for a full description including an analysis of the simulated halos see the original paper by Grand et al. (2017).

2.1.1 Procedure

All the 30 AURIGA halos are selected from the dark-matter only counterpart of the EAGLE simulations (Schaye et al., 2015), where a dark-matter only simulation is run from redshift (z) 137 to the present day. At $z = 0$, halos which have masses similar to the MW halo are selected[2]. In order to find the initial conditions for the re-simulation, the Zal'dovich approximation is used (see Jenkins (2010)): The individual particles of the halo are traced back to their original positions, to reconstruct the area from which the halo formed. This area is then isolated and populated with relatively low mass particles, which increase in mass at greater distance form the center. Then, each dark matter particle is split into a dark matter and a gas particle according to the baryonic mass fraction. The resulting particles have typical resolution[3] masses of $3 \times 10^5\,\mathrm{M}_\odot$ and $5 \times 10^4\,\mathrm{M}_\odot$ for the dark matter and gas particle respectively.

The MHD re-simulations are performed using the AREPO code (Springel, 2010). The code is a so called moving-mesh code, which means at each time step the mesh can be reconstructed to ensure a given target mass. This means that high density regions will be resolved with more cells than low density regions. In addition, the mesh is able to move with the fluid. These features significantly reduce the issues caused by a normal Eulerian fixed grid. A smooth particle hydrodynamics code can also be used to solve these issues, but this requires the introduction of artificial viscosity, something which the moving-mesh code does not need.

2.1.2 Physics Model

The base of the physics model assumes a ΛCDM universe, with cosmological parameters $\Omega_m = 0.307, \Omega_b = 0.048, \Omega_\Lambda = 0.693$ and Hubble constant $H_0 = 100h\mathrm{km\,s^{-1}\,Mpc^{-1}}$ ($h = 0.6777$) found by Planck Collaboration et al. (2014). A full description of the physics model can be found in Vogelsberger et al. (2013), with AURIGA specific decisions in Grand et al. (2017).

Stellar formation is triggered when a gas cell enters a thermally critical regime and star particles are created stochastically, with a decreasing exponential based on a time formation scale of $t_{sf} = 2.2\,\mathrm{Gyr}$. The total mass converted via stellar formation from the gas cell has an upper limit, equal to the average baryonic cell mass ($5 \times 10^4\,\mathrm{M}_\odot$). Each star particle created this way is assumed to be a simple stellar population (SSP), following the Chabrier initial mass function (IMF) (Chabrier, 2003). Stellar feedback for mass loss and metal return is performed via type II and Ia supernovae (SNII and SNIa) and via asymptotic giant branch (AGB) stars. For SNIa and AGB the mass and metals are distributed among nearby cells. The SNII feedback is different, where part of the mass and metals are moved into a wind particle that is launched into a random direction. The contents of the wind particle are deposited back into the gas cells whenever it encounters a low density cell, or has exceeded its maximum travel time. All the energy deposited by the wind particle is split into thermal and kinetic energy to produce a smooth regular wind (Marinacci et al., 2013).

The final feedback mechanism is implemented via black holes, which are seeded in the initial halo. They accrete mass from neighbouring gas cells and via black hole mergers. Energy feedback from a black hole is realised via a radio and a quasar mode. The quasar mode ejects thermal energy isotropically around the black

[2] the selection gives 174 candidates, from which 30 were randomly selected.

[3] This refers to the 'level 4' resolution, the Aurigaia halos have been re-simulated with the higher 'level 3' resolution.

hole, whereas the radio mode heats gas bubbles around the black hole. The bubbles are chosen stochastically with a r^{-2} dependence and the number of heated bubbles depends on the mass accretion of the black hole.

Gas cooling is modeled via a sum of primordial cooling, Compton cooling off the Cosmic Microwave Background and metal dependent cooling. Primordial cooling depends on the initial fraction and mixing of hydrogen and helium. As metals have a lot more transitions than H and He, this increases the cooling rate and hence only primordial cooling is not enough for metal enriched gasses. The metal dependent cooling scales linearly with the metal mass fraction[4] Z. In addition, the H, He, C, N, O, Ne, Mg, Si and Fe elements are traced individually as well. It is possible to calculate the cooling per metal, but this has additional uncertainties, is less efficient and only gives a relatively small improvement. For these reasons, the metal dependent cooling is based off the aggregate Z and not the individual metal abundances.

2.1.3 Data

In total the simulation is run for 30 halos (designated Au1 to Au30), which all have a major galaxy formed at $z = 0$ (end of the simulation). The coordinate systems are oriented such that[5] $(X, Y, Z) = (0, 0, 0)$ is at the center of the large galaxy, with the Z axis pointing along the moment of inertia of the star particles in the inner regions of the halo (this corresponds to the disk rotation). As the star particles represent a SSP their luminosities can be estimated in different bands. In AURIGA the *U, V, B, K, g, r, i* and *z* bands from the Bruzual & Charlot (2003) catalogue are present. These bands allows us to make coloured plots of the star components of all the galaxies (see Figure 3). It is important to note that these magnitudes do not take any extinction or distance into account.

For all of the galaxies, a red spherical bulge-like component has been formed, where most of the galaxies also have a prominent disk. Halos Au11, Au13 and Au30 are exceptions to this, where the first has an imminent merger and the last two seem to have a more spheroidal morphology. Overall, an analysis of the stellar components of the main galaxies show that they are similar to observations of galaxies. For instance, the simulations show flat rotation curves, match the mass-metallicity relations (Gallazzi et al., 2005) and follow present day star formation rates (SFRs). The SFR-stellar mass relation match observations up to $z = 1$, but for higher z seem to be a factor 2 lower compared to observations. The time of the SFR peak is consistent with observations, and occurs between $z = 1$ and $z = 2$. On average, the galaxies are slightly too massive, especially at higher redshifts (like $z = 3$). This could be an indication of stellar feedback being too low early on in the simulation. Around two thirds of the simulated galaxies produce rotationally supported disks, with disk to total mass fractions around $0.6 - 0.7$. This makes AURIGA very useful in studying these late-type galaxies.

2.2 Aurigaia

The AURIGA simulations result in a bunch of star particles representing SSPs, which makes it difficult to compare it to observations looking at individual stars. Moreover, observational challenges like dust extinction, the position and motion of the Sun and, of course, measurement uncertainties. In order to bridge the gap between simulation and observation, a DR2 mock for some of the AURIGA halos has been created, named *Aurigaia* (Grand et al., 2018). Aurigaia contains mocks for halos 6, 16, 21, 23, 24 and 27. Au6 is selected because its properties are close to the MW, Au16 and Au24 have large disks and the remaining halos (Au21, Au23 and Au27) have interesting satellite interactions. A face-on and edge-on luminosity plot of the chosen mock galaxies can be seen in Figure 4. Even though the original resolutions of the AURIGA halos was 'level 4' (Grand et al., 2017), the selected Aurigaia halos have all been (re-)run with the higher "level 3" resolution. The increase in the average dark matter and baryonic mass resolution from level 4 to 3 is roughly a factor 10 (see Table 2 Grand et al., 2017).

2.2.1 The Coordinate System

One of the most important challenges of observing the MW comes from the position of the Sun in the middle of the MW disk. For the mocks, the Sun has been placed at a radius of $R_\odot = 8\,\mathrm{kpc}$ from the galactic center (GC), just above the disk plane with offset $Z_\odot = 0.02\,\mathrm{kpc}$. The default solar position with respect to the central bar is taken to be 30° behind the bar, meaning, starting from the bar semi-major axis, 30° against the disk rotation. There are three other possible positions at an angle of 30° from the bar's semi-major axis, and mocks are available for those as well. Figure 4 shows the locations of the default solar position and the other three options as a cross and plusses respectively. Au24 is a special case that does not seem to have a bar, so the solar orientation is effectively chosen at random. Finally, the galaxy is rotated such that the default solar position in Galactocentric Cartesian coordinates corresponds to $(X, Y, Z) = (R_\odot, 0, Z_\odot)$

[4] Z satisfies $X + Y + Z = 1$, where X and Y are the H and He mass fractions respectively.
[5] note that these X, Y, Z are cartesian coordinates, not the element mass fractions.

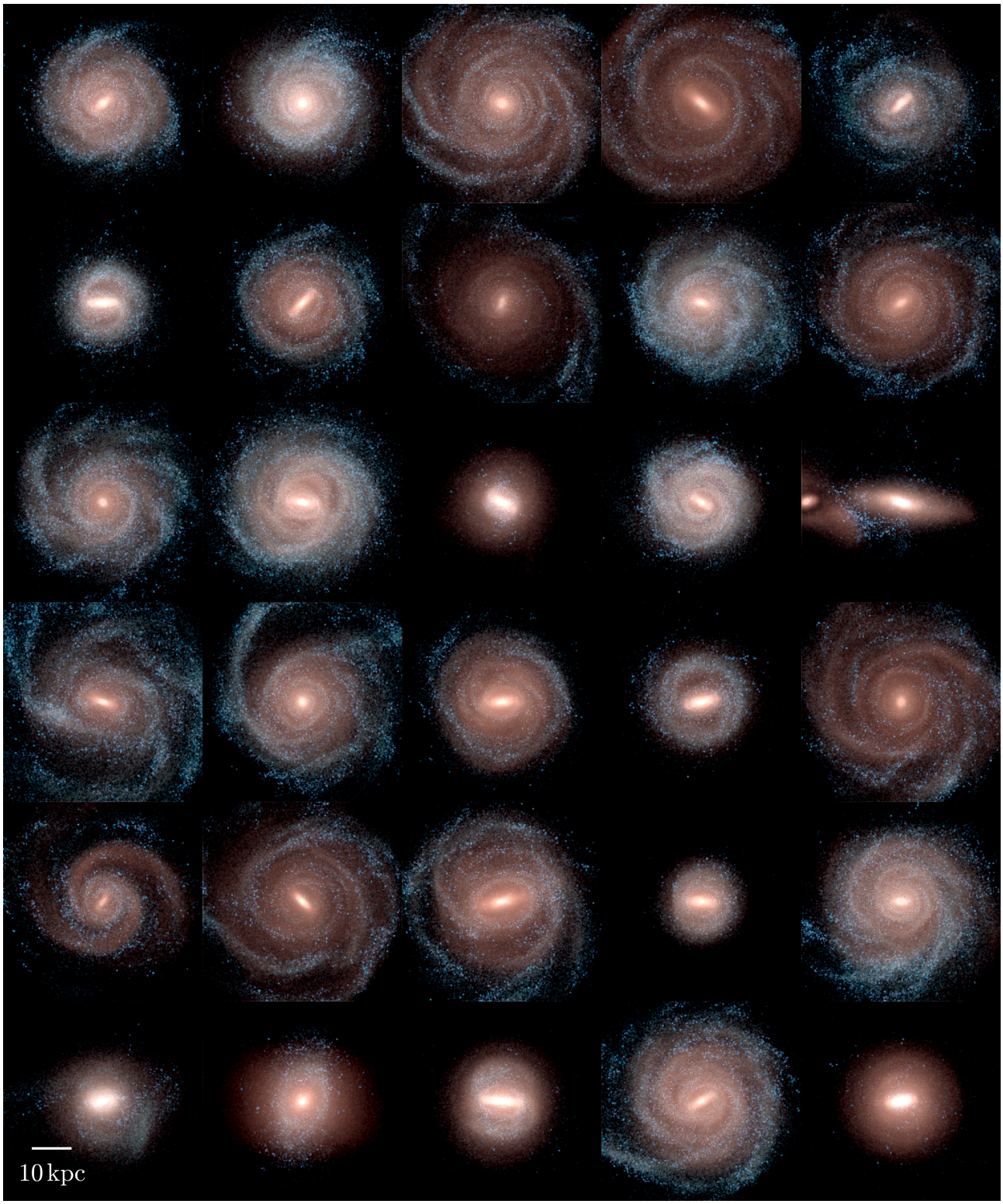

Figure 3: A face-on view of all stellar components of all the individual galaxies. Colours represent the the K-, B- and U bands as red, green and blue respectively. Au1 is the top right image, increasing to from right to left from top to bottom until Au30 in the bottom left corner. Image is taken from the Auriga project homepage http://auriga.h-its.org/

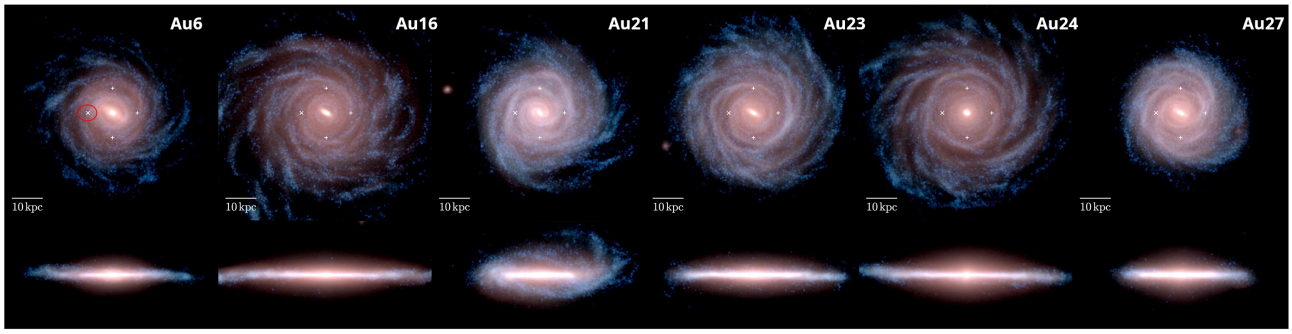

Figure 4: Face-on (top row) and edge-on (bottom row) colour images of all the Aurigaiagalaxies at $z = 0$. The $K-$, $B-$ and $U-$band luminosities are used as the red green and blue colour channels respectively. The white cross (highlighted with a red circle in the left-most image) indicates the default solar position and the white plusses indicate the alternative solar positions. Image taken from Grand et al. (2018), labels and highlight have been added manually.

As the Sun revolves around the GC, it will have an impact on observed quantities. This motion with respect to the GSR can be decomposed into two components: the average motion of stars around the solar position, called the local standard of rest (LSR), and the motion of the Sun with respect to the LSR. The LSR is computed for each galaxy, by spherically averaging the velocities of star particles around the solar position. In general these values (see Table 2) are similar to the MW LSR of $238 \pm 15 \mathrm{km\,s^{-1}}$ (Bland-Hawthorn & Gerhard, 2016). The solar velocity with respect to the LSR is taken to be $(U_\odot, V_\odot, W_\odot) = (11.1, 12.24, 7.25)\,\mathrm{km\,s^{-1}}$, just like our Sun (Schönrich et al., 2010).

The final step is the conversion from Galactocentric Cartesian coordinates (X, Y, Z) to heliocentric equatorial coordinates, right ascension (RA or α) and declination (Dec or δ), which is done following the methods from Hunt & Kawata (2014). These coordinates are then used for the rest of the operations and are the only available coordinates in the catalogues.

2.2.2 Mock Overview

After defining our position in the galaxy and translating the galaxy accordingly, the star particles are expanded into individual stars and other observational effects are applied. Aurigaia has two versions of each mock, that follow slightly different procedures. The HITS-MOCKS use the SNAPDRAGONS code (Hunt et al., 2015), and the ICC-MOCKS use a method from Lowing et al. (2014), but modified for Gaia observables by Mateu et al. (2017). Both methods perform essentially the same steps, apart from one. A general overview of the performed steps is:

1. The star particles are turned into individual stars,
2. MW dust extinction is added,
3. (only ICC-MOCKS) Each star is smoothed over the approximate phase-space of the parent star particle,
4. A cut is made based on the apparent magnitude,
5. Convolve observables with DR2 uncertainties.

There are also alternative mocks created which omit step 2. These are referred to as the NOEX or NOEXT versions of the mocks. We will use the ICC-MOCKS for this thesis, as we are interested in velocities and positions of the stars. The added phase-space smoothing for the ICC-MOCKS makes it a better candidate for this use case. In the next sections, we will describe the steps in more detail and will primarily focus on the ICC-MOCKS.

2.2.3 Stellar Population Synthesis

As the star particles are assumed to be SSPs, it is possible to turn them into individual stars sampling from their IMF and evolving the stars via precomputed isochrones. In the ICC-MOCKS it was possible to use the Chabrier IMF (Chabrier, 2003), which was also assumed by AURIGA. From the SSP initial mass, the expected number of stars is computed in small intervals between masses $0.08\,\mathrm{M_\odot} - 120\,\mathrm{M_\odot}$. In each interval, stars are then drawn from a Poisson distribution using their respective expectation value.

Stellar parameters are then assigned to each of the stars using the PARSEC isochrones. The isochrones are sampled in a grid from age (t) and metallicity (Z). The intervals used are $6.63 \leq \log(t/\mathrm{yr}) \leq 10.12$, with step

size $\Delta \log(t/\mathrm{yr}) = 0.0125$, and $0.0001 \leq Z \leq 0.06$. Instead of interpolating, which turns out to be a difficult task for isochrones, the isochrone for each star is selected based on the closest values for the star's age and metallicity.

2.2.4 Dust Extinction

Extinction for each star is determined from observational MW dust maps. As these are not precisely known, an approximate 3D dust map is created from the observed 2D Schlegel et al. (1998) dust maps (Bland-Hawthorn et al., 2010). The corrected magnitude will then be the original apparent magnitude plus the additional dust extinction based on the star's position in the 3D dust map. An alternative dust map could have been created using the simulated gas distributions, however, making a comparison to Gaia observations would then be more difficult.

2.2.5 Phase-space Smoothing (only ICC-MOCKS)

If the positions of the individual stars are only displaced by the observation uncertainties (like in the HITS-MOCKS), it would be possible for star clumps to form around the parent star particle's original position. To avoid this in the ICC-MOCKS, the 'true' position and velocities (6D phase-space) are assigned individually to each star by sampling from a 6D hyper-ellipsoidal 'smoothing kernel'. This method, which follows Lowing et al. (2014), is able to avoid star clumping, whilst preserving structures like tidal streams. Presevation of these structures is realised by constructing the kernel based on star particles which are born in the same progenitor sub-halo. This method of removing 'cross-talk' between sub-halos, is not guarenteed to work for large scale galaxies, where all stars created in-situ will belong to the same sub-halo group. Kinematic features of in-situ populations can therefore be smoothed out due to this cross-talk, which is exactly the effect we aim to preserve for accreted particles. Theoretically, the unique kinematic features of a small stellar population can be lost if there is a large dominating neighbouring population with different kinematics. Luckily, an example analysis of young disc stars by Grand et al. (2018) does not show a significant bias, but it is still an important effect to keep in mind.

Finally, it is important to remember that this method does not actually add any new dynamical information, nor does it increase the resolution of the simulation.

2.2.6 Magnitude Cuts

To reduce the size of the mocks to around 10^8 stars, some cuts are made in the V magnitude. All stars of apparent, dust-corrected magnitudes $V > 16$ are removed from the catalogue. An exception is made for stars in the halo ($|b| > 20°$), where all stars with $V < 20$ are retained. This exception is made as stars in the halo are generally fainter, and the $V > 16$ cut would lead to a low sample size for halo science.

2.2.7 Gaia DR2 Uncertainties

To make the mock compatible with the Gaia catalogue, specifically Gaia DR2, uncertainties from Gaia are added to all observable quantities. These uncertainties are taken as the post-launch uncertainties, similar to Romero-Gómez et al. (2014). As these uncertainties are end-of-mission estimates and the uncertainties will decrease as the mission goes on ($\propto t^{-1/2}$, for all but the proper motions, which scale $\propto t^{-3/2}$), a correction is made for the DR2 release time. This correction is

$$\sigma_{DR2} = (60/22)^{1/2}\, \sigma_{final},$$

where the fraction corresponds to the DR2 mission time (in months), over the total 5yr mission time. DR2 will only provide radial velocities for a very select set of nearby stars, so the radial velocities in the mock will be available for more stars, in addition to being more accurate than DR2. Uncertainty estimates for atmospheric quantities, like effective temperature T_{eff} and surface gravity $\log g$, are not present in DR2, but are included in the mocks. Their uncertainties are taken from Liu et al. (2012), which estimate them by fitting to synthetic spectra.

The final observed quantities in the mock catalogues are created by displacing the 'true' quantities by a random sample from the corresponding uncertainty.

2.3 Using the Aurigaia Mocks

There are two main ways of accessing the Aurigaia mocks, both working via the AURIGA website[6]. The most convenient access point is the SQL interface, provided by the Virgo Millennium database in Durham[7]. This

[6] http://auriga.h-its.org
[7] http://icc.dur.ac.uk/data/

interface is convenient when only a small sample of stars is needed, hence we initially chose to get the data from here. Unfortunately, the interface was missing multiple key quantities like each star's V-band extinction (keyword: `Extinction31`) and the computed LSR of each halo. As an alternative to the true mocked extinction values, we initially decided to approximate their values by using the Schlegel et al. (1998) dust maps. However, this did not provide us with an accurate enough correction. For this reason, we decided to no longer use the SQL interface.

The alternative option, was to download the complete mock catalogues (as `HDF5` files) and access them locally. Luckily, the ICC-MOCKS with extinction for halos 6, 16, 21, 23 and 24 (all except halo 27) were already downloaded on to the internal Kapteyn system, along with some scripts to access and filter the data. These scripts were written by Tom Callingham (private communication) and are wrappers around the original scripts[8] written by the Aurigaia authors. Some minor modifications were made to run them for our purpose.

In order to avoid reading the entire dataset over and over again, a reduced version of the dataset was made by applying the following cuts:

- $13.5 \leq G \leq 16.5$, similar to the selection made by Arentsen et al. (2020a).
- $|l| < 12^\circ \ \wedge \ |b| < 12^\circ$, creating a -12° to 12° box around the galactic center.[9] The size of this box was chosen in order to include all the observation fields in Arentsen et al. (2020a). For the coordinates of the observed fields see Table 1 in Appendix B.

From now on, we will work with these reduced datasets, which means these cuts are applied for all the following results (see Section 4.1 for a discussion on this magnitude cut). Moreover, due to the availability, we will not work with Au27 and continue with the other halos.

Besides the mock dataset with all the stars (available for all halos), a $z = 0$ snapshot of the original Au6 AURIGA simulation is available on the project homepage as well. This dataset contains more information about the original star particles, like their coordinates of the birth position and specific metal abundances. Crucially, the mock catalogues only contain the metallicity Z (keyword: `Metallicity`), but not the the individual abundances, which we need in order to derive a quantity like [Fe/H]. We can identify the parent star particle of a mocked star by accessing its `ParticleID`, and thereby find the additional information in the snapshot. However, since this snapshot is only available for halo Au6, we have to find an alternative method to compute [Fe/H] for the other halos (see Section 2.3.3).

The processing and analysis will primarily be done with the Python programming language, with standard scientific packages like Numpy[10], Scipy[11] and Matplotlib[12], and Astropy[13] for astronomy specific computations. To work with the large mock datasets we use Vaex[14], which makes use of 'lazy' computations and caching to avoid loading the entire datasets into memory. More information about the code can be found in Appendix C.

2.3.1 Dereddening

To correct the magnitudes for dust extinction, we use the `Extinction31` parameter, given for each star. This parameter corresponds to the extinction in the V-band A_V, which relates the original magnitude m_V with the dereddened magnitude $m_{V,0}$ by (Bradt, 2004):

$$m_{V,0} = m_V - A_V \tag{1}$$

To get the extinction in the Gaia G, BP and RP bands, we use the conversion factors given by Arentsen et al. (2020b):

$$A_G = 0.718 A_V, \quad A_{BP} = 0.9785 A_V, \quad A_{RP} = 0.576 A_V \tag{2}$$

The result of the correction in these filters can be seen in Figure 5.

2.3.2 Velocities to GSR

The radial velocities $v_{r,\odot}$ in the mocks are transformed to the reference frame of the Sun (barycentric). In order to find the radial velocities with respect to the GSR (v_{gsr}), we have to transform them back. The Sun moves with respect to the GSR with velocity $(U_\odot, V_\odot + V_{LSR}, W_\odot)$, (see Section 2.2.1) where the individual compontents are relative to the LSR and the motion of the LSR relative to the GSR (V_{LSR}) is computed for each halo and is in the Y direction. The actual correction is made with Astropy, given the values above.

[8] https://github.com/jchelly/aurigaia-examples

[9] As the dataset only has equatorial coordinates (α, δ), we actually first select everything in $247^\circ \leq \alpha \leq 285^\circ \wedge -46^\circ \leq \delta \leq -12^\circ$ to reduce the size of the dataset. Then we transform the coordinates to galactic coordinates (l, b) and apply the -12° to 12° cut.

[10] https://numpy.org/

[11] https://scipy.org/

[12] https://matplotlib.org/

[13] https://www.astropy.org/

[14] https://vaex.io/docs/index.html

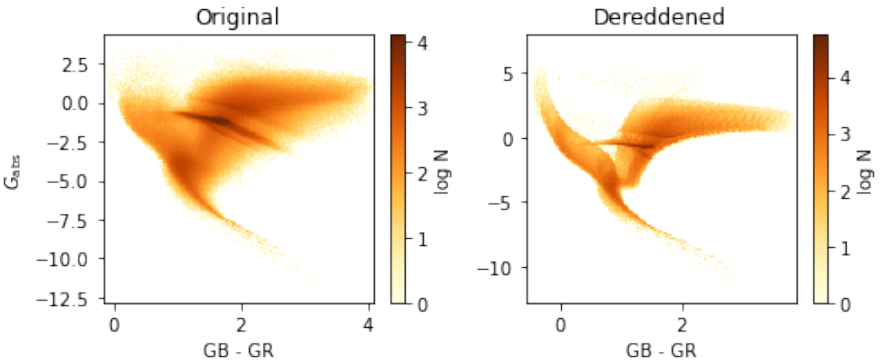

Figure 5: Colour-magnitude diagrams for Au6, where $G_{\rm abs}$ is the absolute G magnitude. Left is the original CMD and right is corrected for dust extinction. The colour of each pixel represents the logged number of stars corresponding to that pixel value.

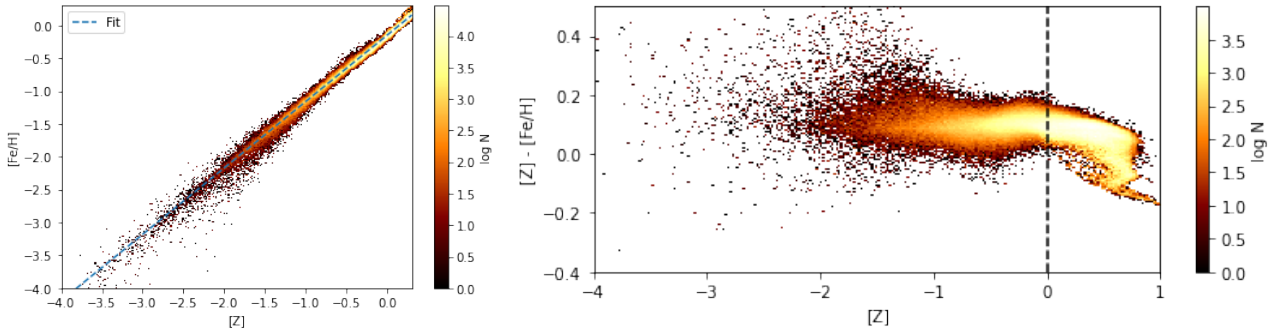

(a) **(b)**

Figure 6: Heatmaps of relative metal mass fraction $[Z]$ and metallicity [Fe/H] in Au6. Left: log heatmap of $[Z]$ − [Fe/H] showing a linear relation between the two, including a linear fit: $[\mathrm{Fe/H}] = 1.0116 \cdot [Z] - 0.1457$. Right: heatmap of $[Z]$ and $[Z]$ − [Fe/H] showing where the relation between $[Z]$ and [Fe/H] is linear (i.e. for $[Z] < 0$). In both figures, the colour indicates the (log) number of stars in the pixel with corresponding $[Z]$ and [Fe/H].

2.3.3 Deriving Metallicity

The observations of Arentsen et al. (2020a) have been made in different [Fe/H] bins, so in order to reproduce them we have to compute these values as well. As described in Section 2.3, only the total mass fraction of metals Z is given in the mocks, so we have to find a conversion between Z and [Fe/H]. It is possible to use an observed relation as this conversion factor, but we can derive our own relation with [Fe/H] known in one of our halos. Au6 is the only halo where an AURIGA snapshot at $z = 0$ is given, which includes the abundances of all traced elements: H, He, C, N, O, Ne, Mg, Si and Fe. By deriving a conversion factor based on Au6, we implicitly use the relation between the elements as a result of the assumptions made by AURIGA on supernovae and chemical enrichment. As the same assumptions are made in the other AURIGA halos, we can therefore apply this relation to them as well, assuming a similar chemical evolution.

To find the conversion factor, we first compute [Fe/H] from the snapshot abundances using:

$$[\mathrm{Fe/H}] = \log\left(N_{Fe}/N_H\right)_\star - \log\left(N_{Fe}/N_H\right)_\odot \tag{3}$$

or, with $\log \varepsilon_X = \log\left(N_X/N_H\right) + 12$

$$[\mathrm{Fe/H}] = \log\left(N_{Fe}/N_H\right)_\star - \left(\log \varepsilon_{Fe} - 12\right) \tag{4}$$

where $\log \varepsilon_{Fe} = 7.50 \pm 0.04$ in our sun (Asplund et al., 2009). Now, we also compute the total metal mass fraction with respect to the solar mass fraction:

$$[Z] \equiv \log Z_\star - \log Z_\odot \tag{5}$$

with $Z_\odot = 0.0153$ (Caffau et al., 2011). We now plot $[Z]$ against [Fe/H] (see Figure 6a) and notice that there seems to be a linear dependence between them. To further investigate this dependence, we look into the difference between [Fe/H] and $[Z]$ as a function of $[Z]$ (see Figure 6b). Here we see that for $[Z] < 0$ the dependence does have quite some spread, but roughly follows a straight line with approximately 0.1 offset from 0. For $[Z] > 0$ we see a very sharp decrease, which is caused by the onset of SNIa which mainly produces Fe over other metals. From this, we decide to fit a linear relation

$$[\text{Fe/H}] = a \cdot [Z] + b \tag{6}$$

for $[Z] < 0$ using linear least squares, giving

$$a = 1.0116 \pm 0.0007 \qquad b = -0.1457 \pm 0.0003 \tag{7}$$

The fit is also overplotted in Figure 6a. As we expected from the $[Z]$ to $[Z] - [\text{Fe/H}]$ relation, the slope a is very close to 1, and we have an offset of $b \approx 0.15$. With this fit, we can now find metallicities for the other halos. To be consistent across our analysis, from now on we will also use the fitted [Fe/H] values for Au6 and not the ones computed from the snapshot abundances.

2.4 Analysis

Now that we have the mocks and applied some general operations, we can perform our analysis. The analysis is split into four parts: First we try to recreate the observations from Arentsen et al. (2020a) using Aurigaia, by applying similar observation selections to Au6. Then we will adjust these selections to investigate wether they impact the observed pattern. From that point on, we will investigate the remaining halos and compare the patterns to Au6, considering the different properties between these galaxies. Finally, we will look into potential causes for what we observe.

Alongside making plots similar to Arentsen et al. (2020a) (see Figures 1 and 2), and qualitatively comparing the 'flattening', we also quantify this relation by using a measure of observed rotation. We can define the rotation as being equal to the slope R in the proportial longitude, $\overline{v}_{\text{gsr}}$ relation:

$$\overline{v}_{\text{gsr}} = R \cdot l \tag{8}$$

Given l and $\overline{v}_{\text{gsr}}$, we can fit R using linear least squares, and then use R to quantitatively compare between metallicity bins and galaxies. There will be cases where the $\overline{v}_{\text{gsr}}$ is not related to l at all, and the fit will not have a lot of meaning. This will be reflected, however, in the error in the fit ΔR, also given by linear least squares.

As a reference to the milky way bar rotation, we use simulated model fits for the bar pattern on BRAVA (Rich et al., 2007) data from Shen et al. (2010). Note that no specific population is observed in this survey, and hence metal rich stars will dominate. The model will therefore be less relevant for more metal-poor populations, as is seen by Arentsen et al. (2020a).

2.4.1 Reproducing Observations

In order to reproduce the observations of Arentsen et al. (2020a), we apply the same selection effects and cuts to the MW analogue Au6. The following cuts are made:

(i) G magnitude in the range $13.5 < G < 16.5$, which we already do when we retrieve the data.

(ii) According to Arentsen et al. (2020b), a selection on colour $BP - RP$ is made, however the exact values are not given. From figure 2 in Arentsen et al. (2020b), we can roughly estimate the range to be $0.4 < (BP - RP) < 1.4$.

(iii) A parallax (π) cut is made as well, to remove stars close to the Sun. This cut removes all stars with $\pi > 0.000\,25''$, corresponding to a distance smaller than 4kpc.

(iv) To remove bright giant stars behind and dwarfs in front of the GC, a cut in surface gravity ($\log g$) is made as well. Only everything in the range $1.8 < \log g < 3.2$ is retained. Additionally, Arentsen et al. (2020a) remove horizontal branch (HB) stars by the cutting everything under the line $\log g = T_{eff}/480 - 8.1$. Performing this cut for us resulted in a significant reduction of metal poor stars. HB stars are mainly removed because the spectroscopic analysis method applied by Arentsen et al. (2020a) cannot deal with them as accurately as it can for red giants. Therefore, the resulting [Fe/H] and T_{eff} would not be reliable for this population. As we do not have this constraint, and do not expect the HB stars to be kinematically different, we chose not to apply this cut.

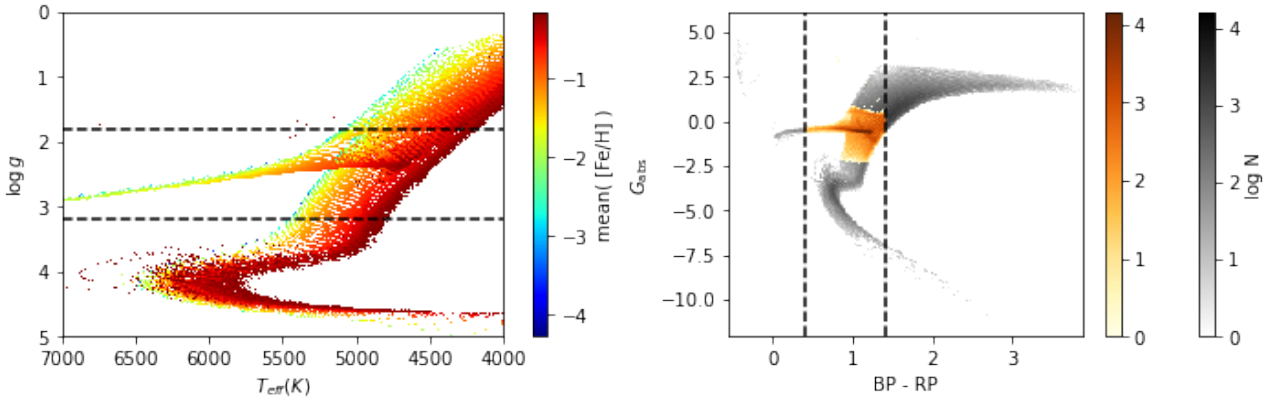

Figure 7: Left: $T_{\rm eff} - \log g$ diagram, where the colour indicates the mean [Fe/H] of the stars in the pixel. The horizontal lines show the $\log g$ cuts at 1.6 and 3.2. Right: a dereddened colour magnitude diagram, showing which parts are cut with the observational selection effects. Orange colours are included, gray values are cut away. The vertical lines show the cuts in $GB - GR$ at 0.4 and 1.4.

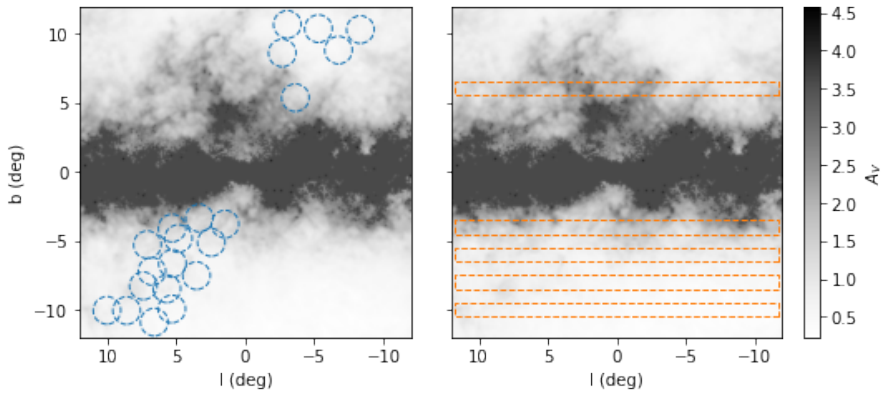

Figure 8: The observation fields from Arentsen et al. (2020a) (left) and the latitude selection cuts (right) displayed over the mean extinction A_V in each pixel. When no stars were present in a pixel (i.e. around $b = 0°$), A_V is taken as the max A_V value in the image.

(v) The observations of Arentsen et al. (2020a) are performed from the Northern hemisphere, which means all the fields have $\delta > -30°$. To stay consistent, we only select stars in the 1° fields from the observations. The locations and sizes of the fields can be seen in Figure 8. Precise coordinates of the center of all fields can be found in Table 1 in Appendix B.

All the above cuts are applied on observed quantities (i.e. the ones that have been convoluted with the Gaia DR2 errors), with an exception for spectroscopic parameters (like surface gravity) as the ones derived by Arentsen et al. (2020a) have much higher quality than the ones from DR2. A visual representation of all the main cuts on our population of stars can be seen in Figure 7.

2.4.2 Selection Effects

In order to see if the pattern is an artifact from observational selections, we will create the same plots with other selections. For each of these, we do not make any of the selections described in the previous section (Section 2.4.1), unless stated explicitly (except for the general magnitude cut (i), which is applied everywhere). We investigate the following selection effects:

1. We see if the location of the observation fields has any effect, so we now consider the entire -12° to 12° box (referred to as the 'selection box'). The other selection effects (i, ii, iii and iv) are still applied on the observed values.

2. We constrain the selection to strips of fixed latitude, similar to what is done in surveys like BRAVA (Rich et al., 2007; Kunder et al., 2012). We consider strips at latitudes $b = 6°, -4°, -6°, -8°, -10°$ all with

$\Delta b = 0.5°$, resulting in rectangular strips of side 1 and stretching across the entire longitude range (see Figure 8).

3. We then want to see what the effect is of the uncertainties on the selections we make. So we again look at the entire box, but this time make the other selections on the true parameters instead.

4. We test if foreground and background stars have a significant effect on the observed patters. To see this, we look at the entire box but now select stars based on their true Galactocentric Cartesian coordinates. We keep everything in the cylinder around the GC, with a radius of 4kpc ($R_{\rm disk} = \sqrt{X^2 + Y^2} < 4$kpc) and height of 1kpc ($|Z| < 1$kpc). We do not make any of the other cuts here.

5. To see the effect of turning the star particles into individual stars, we recombine the stars into their parent AURIGA star particles. This is done by grouping the stars by their parent particle (`ParticleID`) and take the position and radial velocity of this star particle as the mean respective quantities of the grouped stars. A star particle has a single metallicity, which is then equal for all stars, hence we do not have to combine this in a special way.

2.4.3 Looking at Other Halos

So far, we have focused our attention to the MW analogue Au6, but now we also look at the patterns in the other halos (Au16, Au21, Au23 and Au24). There are some interesting differences between these halos and the MW analogue Au6. Au16 and Au24 have been included in Aurigaia due to their large disk size, and Au21 and Au23 because of interesting satellite interactions. Moreover, Au6 appears to have the largest fraction of accreted stars in the bulge ($\sim 14\%$), where Au16 Au23 and Au24 all have very low fractions ($< 4\%$) (Gargiulo et al., 2019).

An analysis of the bulges in AURIGA showed that all of them can be classified a PsB, but some have an additional spherical ClB component (Gargiulo et al., 2019). Five of the AURIGA galaxies have a definite B/P bulge, among them Au23 (Blázquez-Calero et al., 2019). Notably our MW analogue Au6 appears not to have a B/P, contrary to the observational evidence of the MW (Barbuy et al., 2018). From a visual inspection (Figure 4), we can see that Au24 has a very spherical bulge, but it is still classified as a PsB.

Moreover, the formation histories of the galaxies differs as well, Au21 and Au24 have some relatively recent mergers (~ 4 Gyr ago) in addition to some big mergers around 8 Gyr, the other halos also undergo mergers, but they are more spread out over time and less massive (Gargiulo et al., 2019).

2.4.4 Potential Causes

Since we are looking at a simulation, we have some additional information available to us which can help us investigate the pattern, and give us insight into potential causes for the decreasing slope. An important property of the star is whether is has been born in-situ or ex-situ and has been accreted in a merger. For each star we have an `AccretedFlag` which gives us this information, so we can make similar relations but with the accreted and in-situ populations separated. As we have a AURIGA snapshot available for Au6, we also know the birth positions of each star particle in this halo and can investigate where the stars come from. With this we can see if the accreted particles come from a few big mergers, or from many little mergers.

Another interesting property is the actual `Age` of the star, which is essentially what we are trying to probe by looking at low [Fe/H]. We can therefore recreate the same $l - \overline{v}_{\rm gsr}$ relations, but with the stars binned by their age, instead of metallicity. With this we can also check if [Fe/H] is indeed a good indicator for the star's age. In addition, we also include the times of some of the major mergers, taken from Gargiulo et al. (2019). With this information, we can see if there is a relation between major mergers and the degree of flattening as is indicated by Fragkoudi et al. (2020).

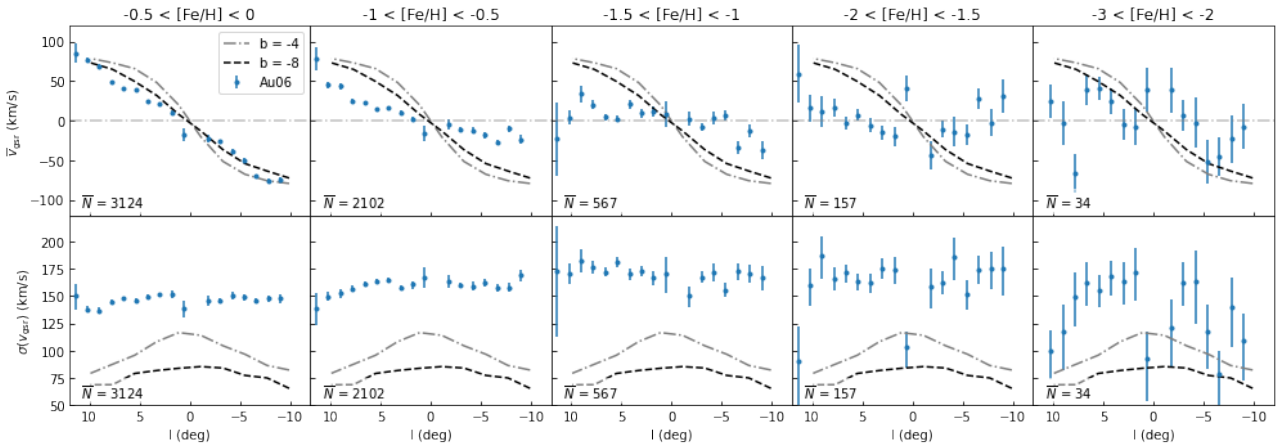

Figure 9: Top row: longitude ($\Delta l = 1.2°$) versus mean radial velocity in GSR ($\overline{v}_{\rm gsr}$) for specific metallicity ([Fe/H]) intervals in each column, decreasing from left to right. Error bars are $\sigma/\sqrt{N}$. Bottom row: similar to top row, but with standard deviation (i.e. dispersion) of radial velocity. The (asymmetric) error bars are $\sqrt{\sigma^2(N-1)/\chi^2_{\pm}}$, with $\chi_{\pm}$ determined for a 68% confidence interval and $N-1$ degrees of freedom. In both rows, stars have been selected from halo Au6, using observational selections similar to Arentsen et al. (2020a). The MW models for a B/P bulge from Shen et al. (2010) have been overplotted.

3 Results

3.1 Recreating Observations

In Figure 9 we show the results for Au6 with all the observational selection effects applied (Section 3.1). Similar to Arentsen et al. (2020a), we include the Shen et al. (2010) fits for the MW B/P bulge at latitudes $b = -4°, -8°$ as reference as well.

When we compare this to the result of Arentsen et al. (2020a), also seen in Figure 10, we see a very similar pattern: In the most metal-rich bin, the $\overline{v}_{\rm gsr}$ follow a specific pattern along l, roughly matching that of the MW bulge. Then, as we go towards lower metallicity bins ([Fe/H] : -0.5 to -1 and -1 to -1.5), the pattern first flattens and finally in the extremely metal-poor bins the uncertainties dominate and we do not see a pattern anymore. When we fit the slope R (see Section 2.4) and plot them for each bin (Figure 11a), we can quantify this effect.

For the velocity dispersions $\sigma(v_{\rm gsr})$ (Figure 9 row 2), however, we do see quite a significant difference compared to the observations, where the $\sigma(v_{\rm gsr})$ does not seem to increase at all towards lower metallicities. In the metal-rich bins the dispersions seem to be significantly higher than the MW observations, whereas in the metal-poor bins the uncertainties dominate. When we look at the [Fe/H] $-$ $\sigma(v_{\rm gsr})$ relation for all l combined (Figure 11b), the pattern is drastically different from the observations, as we do not observe a linear relation at all. We do see that at the lowest metallicites [Fe/H] < -2, the velocity dispersions do seem to match the observed values.

Another difference with respect to Arentsen et al. (2020a) is that we also include the metal-rich [Fe/H] 0 to -0.5 bin, so the 'left-most' bin in Arentsen et al. (2020a) corresponds to our second bin. Note, that the slope in the observation in this bin of Arentsen et al. (2020a) is actually steeper than what we see in Au6.

3.2 Selection Effects

We now look into the observational selections and their effect on the observed pattern, as outlined in Section 2.4.2. We first look at selection effects 1, 3 - 5 (i.e. everything except the latitude strips). The complete $l - \overline{v}_{\rm gsr}$ relation for each of the bins and selection effects can be seen in Figure 12 and a similar plot for $\sigma(v_{\rm gsr})$ can be seen in Figure 13. A more condensed view of these plots is made by fitting the slope in each bin for the mean velocities (Figure 14a) and by computing $\sigma(v_{\rm gsr})$ across all l (Figure 14b). For all these figures, a condensed description of the selection is given as its label. The area selection is either the entire *Box* or just the observational *Fields*. The other cut is made on either the uncertainty convoluted parameters (*Obs*), the *True* parameters or on based on the true position in the bulge (*Pos*). Finally, when the stars are combined into

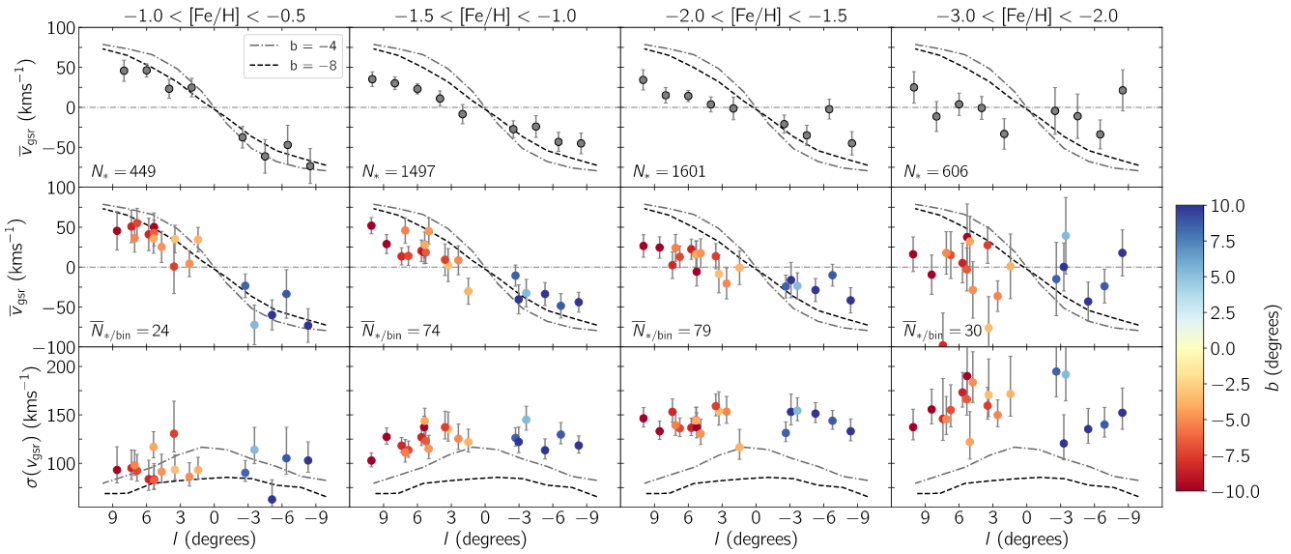

Figure 10: Results from Arentsen et al. (2020a), identical to Figure 1, it is included here for an easier comparison with Figure 9.

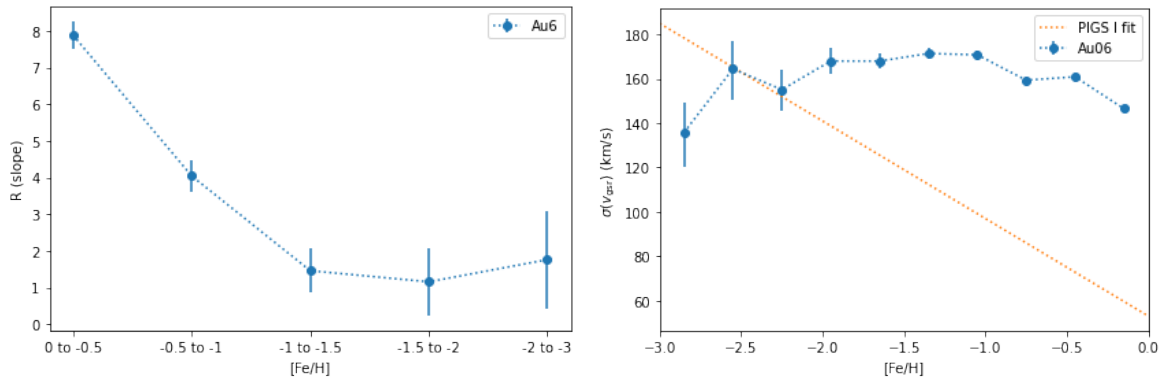

(a) **(b)**

Figure 11: (a): Fitted slopes (R) from the $l - \overline{v}_{\mathrm{gsr}}$ relation shown in Figure 9 in the corresponding metallicity intervals. Error bars are given by the standard error in the fit $\sqrt{\Sigma r_i^2/[(N-1)\Sigma l_i^2]}$, where r_i are the residuals of the fit. (b): Standard deviations in the radial velocity in GSR over the entire longitude range (-12° to 12°) for metallicity bins of size 0.3dex. Overplotted is the approximate fit (slope −44dex) of the observed values for this relation from Arentsen et al. (2020a), where we estimated the offset by eye. The (asymmetric) error bars are $\sqrt{\sigma^2(N-1)/\chi^2_{\pm}}$, with $\chi_{\pm}$ determined for a 68% confidence interval and $N-1$ degrees of freedom.

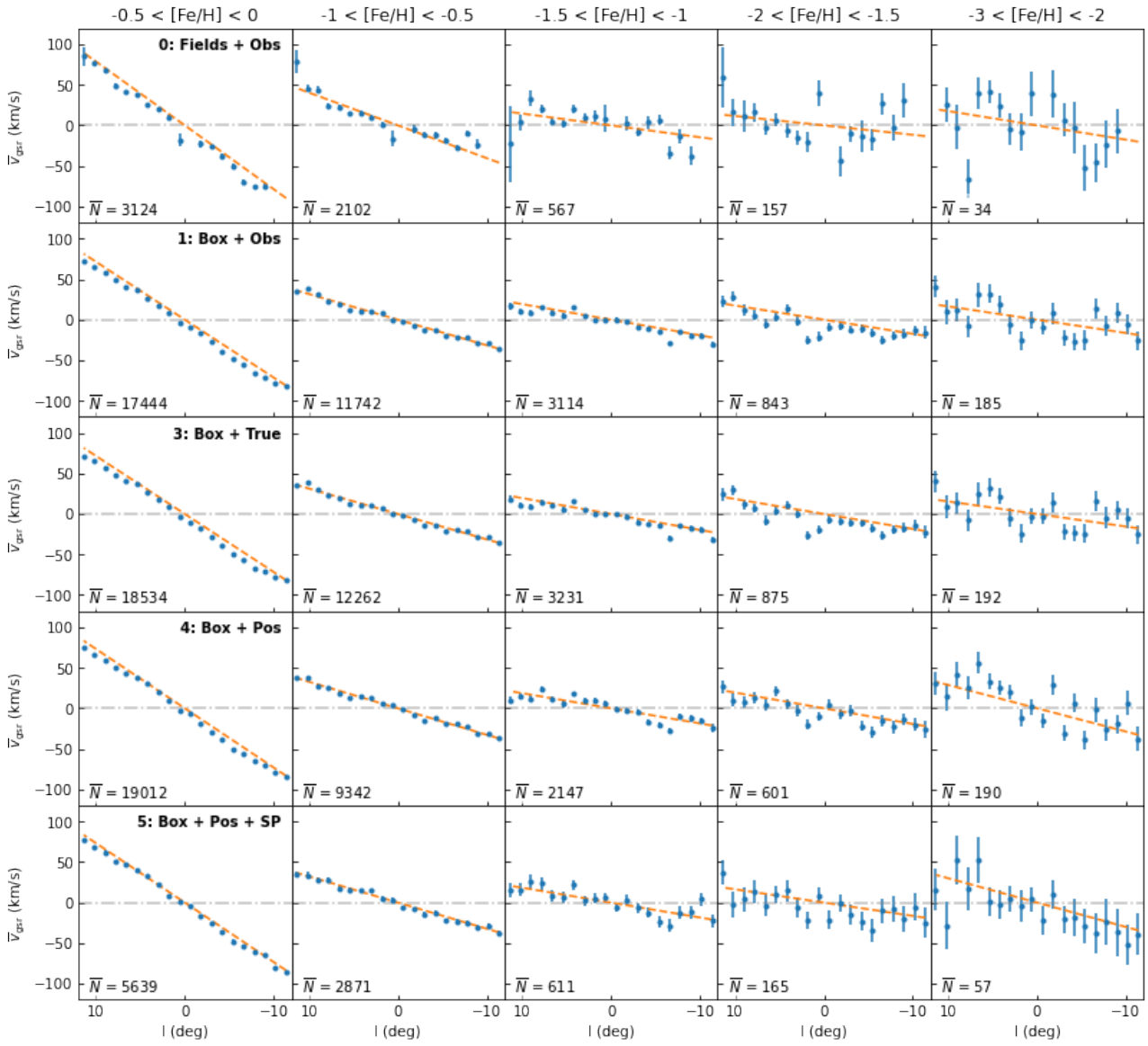

Figure 12: Similar to first row of Figure 9, but with the rows indicating different selection strategies, the slope fit $\overline{v}_{\rm gsr} = R \cdot l$ as the orange dashed line and without the MW Shen et al. (2010) models. All data is from halo Au6. The different selections are indicated in the top right of the first row: *Box* or *Fields* indicates the selection used for location. *Obs*, *True* or *Pos* indicates whether cuts have been made on 'observed' or true parameters, or based on the true position in the bulge. *SP* indicates that stars have been recombined into their parent star particle.

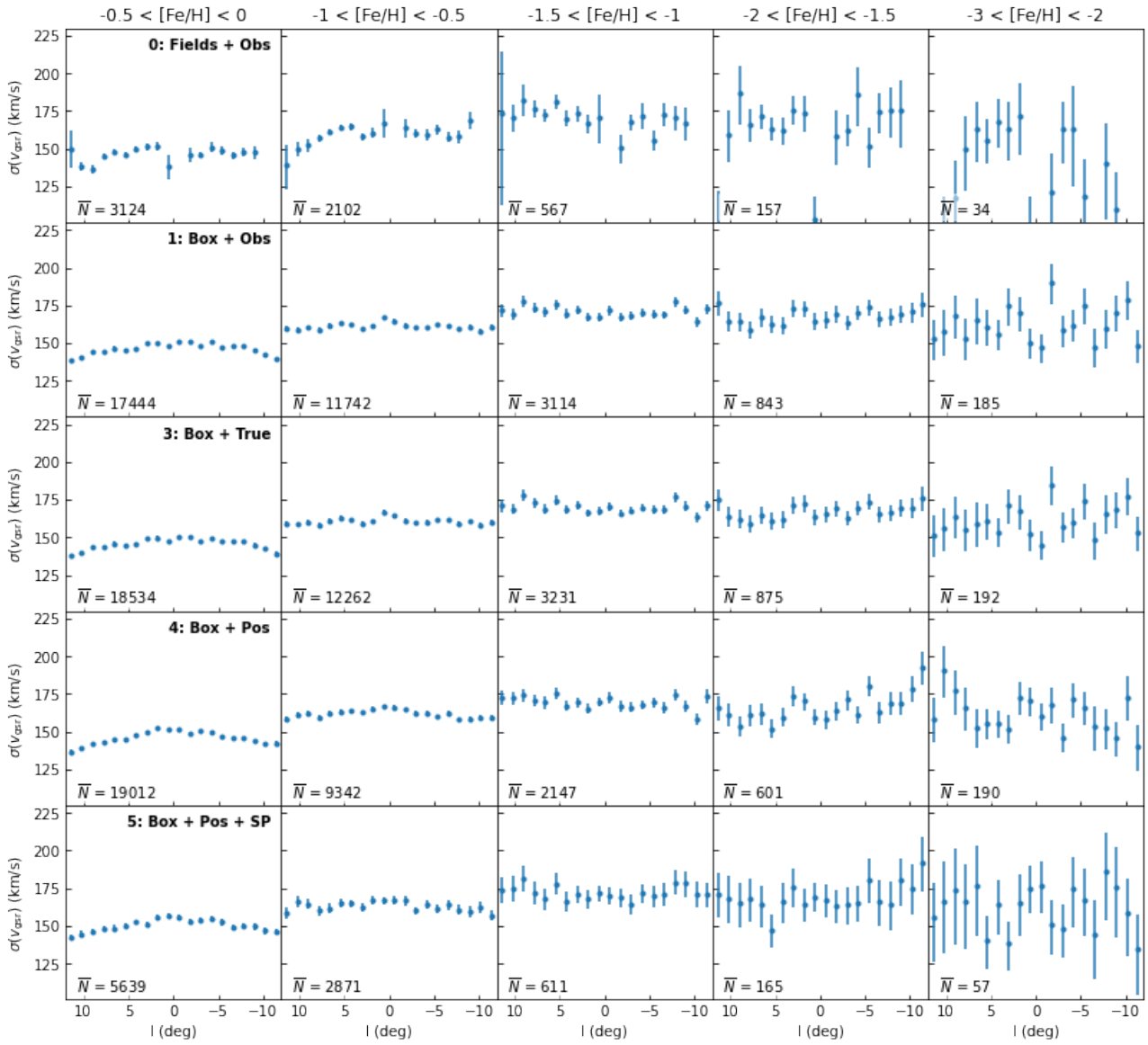

Figure 13: Similar to Figure 12, but with velocity dispersions from Au6, like in row 2 of Figure 9.

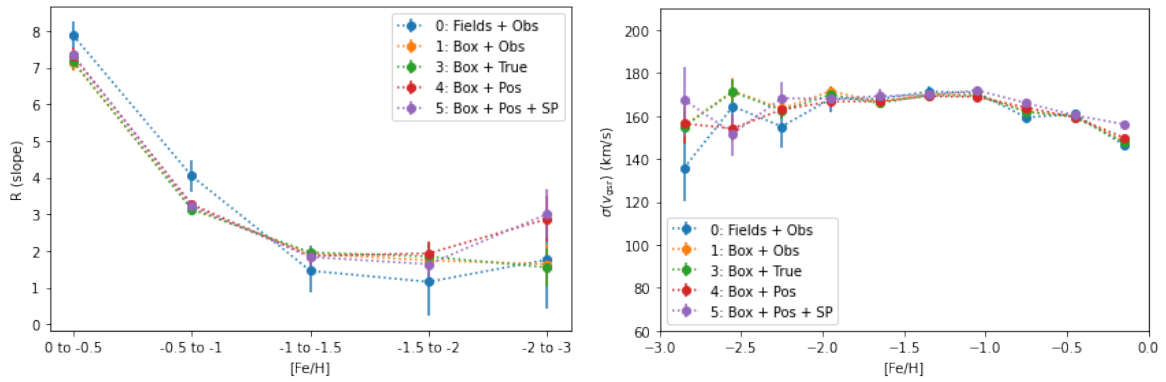

(a) **(b)**

Figure 14: Similar to Figure 11, but for all data from different selections in Au6. For (a) see Figure 12, and for (b) see Figure 13.

their parent star particle, it is designated with *SP*. For more details, we refer to Section 2.4.2. The numbers in the labels also correspond to the selection item numbers in this sections. For reference, the selection applied for recreating the observations (Section 2.4.1) has been included in these figures, and is given the number 0.

From the figures, we can essentially conclude that the selections do not have a significant impact on the overall flattening pattern. When we take a look at the average number of stars in a l bin $\overline{N}$ (like Figure 12 bottom left in each plot) we see that the selections on the entire box have roughly five times as much data points, compared to the observational selection (first row). This is expected, as the area in which stars are selected is simply larger, and the increased sample size therefore gives a lower spread in the datapoints. For the fitted slopes (Figure 14a), we see that the observational selection has a higher slope for the metal-rich bins and is lower for the intermediate and metal-poor bins. In the last bin, there seems to be a split between selections 1,3 and 4,5. The difference between these selections is that the first two use stellar parameters (like $\log g$) to cut foreground and background stars, whereas 4 and 5 use the true positions from the simulation. From this it seems that potential foreground and background stars can decrease the slope in this bin, but it is hard to put a firm conclusion on this due to the high uncertainties in this bin. One would expect that when the effect of non-bulge stars is strong, it would also be visible in the other bins. However, as we do not see this it is likely an effect of the lower sample sizes in this extremely metal-poor bin.

The picture for the dispersions is very similar to that from the mean velocities; the increased sample size due to the larger selection areas reveals a more curved pattern in the most metal-rich bin in Figure 13, similar to the models from Shen et al. (2010). Still, these dispersions are a lot higher than the MW observations and the selections essentially do not seem to have any impact on them, as the [Fe/H] $-$ $\sigma(v_{\rm gsr})$ relation does not change significantly for the different selection effects.

To check that our results are not an artifact of the perceived increase in resolution due to the expansion of star particles into stars, we look at selection 5 in more depth. In this selection we first combine the stars back into their parent star particle and then select all particles in the box which are located in the bulge. In Figure 14 we see no difference between this selection and the other selections, which is a good sign. The mosaic figures do show that the uncertainties for each datapoint are larger than the other selections, which is mainly due to the lowering of sample sizes. We see that the locations of the datapoints do not differ a lot from the locations of the other selections.

3.2.1 Horizontal Selection Strips

Finally, we take a look at the effect of the selection strips (selection 2), which can be seen in Figure 15. The ranges in these figures are a bit different due to the higher spread in the low metallicity bins. When we look at the average l bin size, we see that for the extremely metal-poor bins they are around 10 stars (with $b = 6°$ and $b = -4°$ even lower). This is significantly lower than all our other selections, where the worst case was $\overline{N} = 33$ for the observational recreation (selection 0). The low sample sizes in these bins will result in high uncertainties in the datapoints and consequently in an unreliable fit. However as the R fit is not weighted by uncertainty in the datapoints, this is not directly reflected in the error bars of the fit. The spread we see in these lowest metallicity bins is therefore explained by the low sample sizes. In the metal-rich bins, we see that the values for R are similar to all the other selections ($R_{[0,-0.5]} \sim 7$ and $R_{[-0.5,-1.0]} \sim 3-4$). We therefore conclude that, apart from the number of selected stars, this selection also does not have a very significant effect on the overall pattern. The full mosaics can be seen in Appendix A, Figures 26 and 27.

In summary, we do not notice any significant effect due to the different selections. Both in the selection coordinates and in observed versus true quantities we see that the pattern of flattening towards metal-poor populations is unchanged. We did see that by looking at the stars instead of the star particles, the uncertainties artificially decrease so we should consider them as a lower estimate. In order to not complicate the analysis, we now proceed with only selection 3 (entire box plus the true bulge selection), as this selection has the highest sample size and we can be sure that we have no foreground or background stars in our sample.

3.3 Other Halos

After looking at Au6 and various selection effects on this halo, we now extend our analysis to the other halos in Aurigaia. Figure 16a shows the fitted slopes for each halo across all the metallicity populations. Figure 16b contains the combined velocity dispersions across all longitudes as a function of metallicity for all Aurigaia halos. The full images with the means and dispersions for all l in each bin for each halo can be found in Appendix A, Figures 28 and 29. We first consider at each galaxy individually and then discuss the general trends in bulge rotation and velocity dispersions:

Au6 This galaxy is our MW analogue with a PsB, but notably does not seem to have a B/P bulge (Blázquez-Calero et al., 2019). Compared to the other halos, it has the highest fraction of accreted stars in the bulge, which is around 14%. Its merger history seems the be average compared to the other galaxies' merger

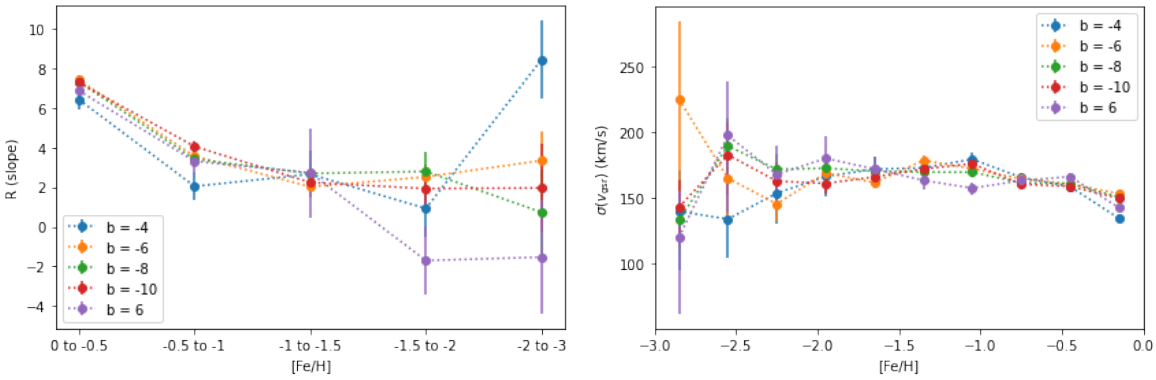

(a) **(b)**

Figure 15: Similar to Figure 14, but for different selections of stars located at specific galactic latitude strips. The center is indicated by b (in degrees) and each strip has a width of $\Delta b = 1°$ and stretches along all longitude (see Figure 8). The full mosaics of the respective selections can be found in Appendix A, Figures 26 and 27.

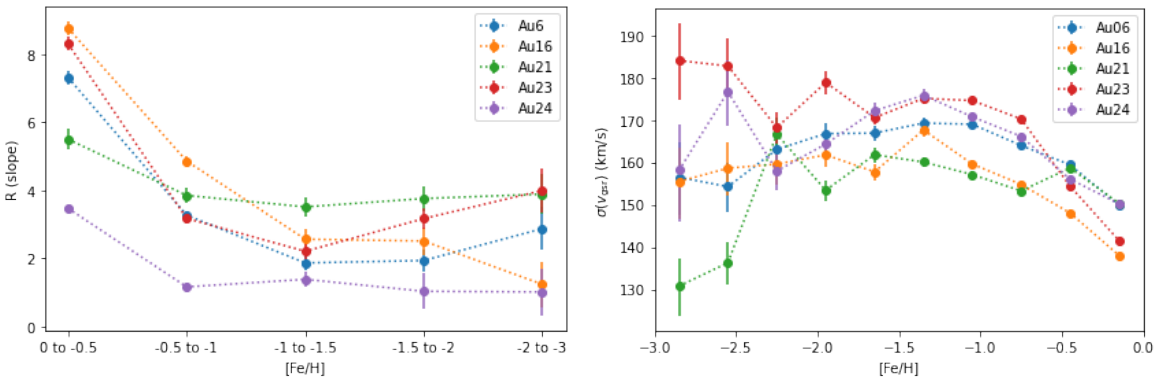

(a) **(b)**

Figure 16: Similar to Figure 11, but for all halos. The selection used for all the halo uses the full box and stars with true positions in the bulge. The full mosaics of individual halos can be found in Appendix A, Figures 28 and 29.

histories. We already saw the rotational fall-off of this galaxy in the previous sections, where the slope is high in the metal-rich bin and falls off until the $[-1, -1.5]$ bin whereafter it flattens out. Its dispersions seem to increase slightly until [Fe/H] ≈ -1.3 and then decrease again.

Au16 This galaxy was included in Aurigaia for its large disk, since it has a stellar disk scale radius of $R_d = 6.0$kpc (Grand et al., 2018) which is roughly twice the MW value of $R_d = 2.6 \pm 0.5$kpc (Bland-Hawthorn & Gerhard, 2016). It has a low fraction of accreted stars (1%), as it had a relatively quiet merger history (Gargiulo et al., 2019). We see (Figure 16a) that it has one of the fastest rotation in the bulge, similarly falling off until metallicity $[-1, -1.5]$ and then flattening out. It has the lowest velocity dispersion at high metallicity but its overall pattern is similar to Au6.

Au21 This galaxy has been included due to its interesting satellite interactions, which includes two major merger events at $t = 8$ Gyr (where $t = 0$ is now) and one at $t = 2.2$ Gyr (Gargiulo et al., 2019). Its disk seems to have a similar size to Au6, but hass more stellar mass. Au21 seems to have a relatively low rotation at high metallicity, but also flattens out much earlier (at $[-0.5, -1]$). The velocity dispersions of this galaxy seem to fluctuate more across the metallicities, and drops towards the very metal-poor regime.

Au23 Similar to A21, it has been included due to interesting satellite interactions, but it seems to have had almost no merger events after $t = 10$ Gyr apart from a recent one around $t = 4$ Gyr. A23 has the only bulge that has been designated as a B/P bulge by Blázquez-Calero et al. (2019). Its rotation patterns are very similar to Au16, but it seems to fall-off a bit faster. Towards lower metallicities it increases again, but here the uncertainties are also quite big so we cannot conclude too much from this.

Au24 Finally, this is another large disk galaxy similar to Au16 but also has had a much more active merger history. Just after $t = 9$ Gyr three merger events happend in close succession, and a final event occured at $t = 4$ Gyr (Gargiulo et al., 2019). Bulge in this galaxy also does not appear to have a very strong bar (Figure 4), but it has been classified as a PsB by Gargiulo et al. (2019). In the rotation slopes, we see that indeed it has the lowest rotation in the most metal-poor bin. Its rotation then almost vanished in the following bin, and stays constant thereafter. The velocity dispersions of Au24 appear to be pretty similar to Au6.

Combining all this information, we can make two rough groups from the rotation bulge rotation strength (Figure 16a). The first group (Au6, Au16 and Au23) have high rotation in the metal-rich bin and then decreases until the third bin ($[-1, -1.5]$). Au16 and Au24 have significantly lower initial rotation, and only fall-off until the second bin ($[-0.5, -1]$). Both galaxies then have a very constant slope towards lower metallicity populations. Notably, the galaxies in the second group seem to have had some very strong merger events in its history, where the other group's merger history was relatively quiescent. We will further explore this relation in the following section.

The velocity dispersions (Figure 29) seem to be roughly the same for all halos, where there is a small increase from [Fe/H] 0 to ~ -1.5. After this point, there is no clear pattern anymore, which is likely attributed to the uncertainties in these bins. It is hard to really group halos here, apart from the fact that the highest slope halos (Au16 and Au23) correspond to the lowest $\sigma(v_{\rm gsr})$ values in the metal-rich regime. However, this does not hold for any of the lower bins.

From these results, we can conclude that the flattening towards metal poor populations is visible in a variety of galaxies with PsBs and with varying disk sizes. Au24 is the only galaxy in the mocks that has a clear spherical shaped bulge, but we see that there still is some rotation in the galactic plane. Even though the rotation is weaker in this halo, we still see the slope decrease towards lower metallicities.

3.4 Merger History and Stellar Ages

To look more into the causes of the observed differences in rotational fall-off, we investigate some additional quantities which are given from the simulations. For halo Au6, the $z = 0$ AURIGA snapshot gives us the birth position of each star particle, which we can visualize as a function of formation time. In Figure 17, we plot the distance (in Mpc) of the birth position of the star particle from the center of the main galaxy as a function of the age of the star. Note that $t = 0$ is now, so time goes forward as the y-axis goes down. The figure is split into in-situ and accreted particles by colour. We can nicely see that multiple mergers happen in this galaxy, especially some big ones in the early times of the galaxy. Figure 18 splits the previous figure up into the different metallicity intervals. Here we see that essentially all the very metal-poor stars are formed very early on and mostly in the satellites of Au6. Notably, these metal-poor populations are then accreted at later times, so we would expect that there is a kinematic difference between in-situ and accreted metal-poor populations.

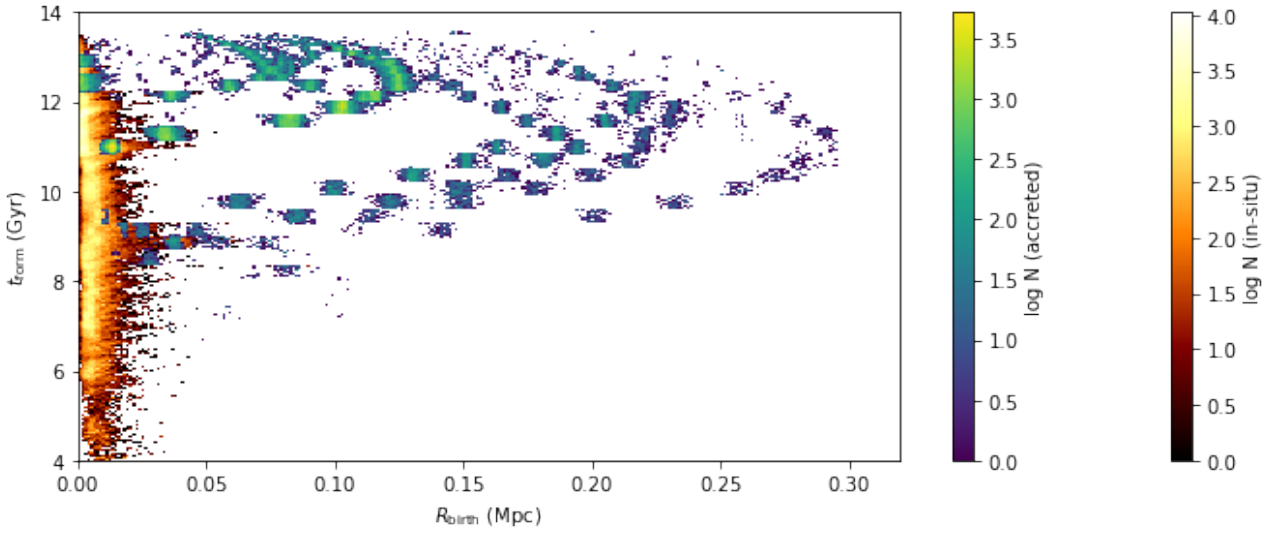

Figure 17: Heatmap of the birth radius of the stars in the Au6 bulge and the age (or formation time) of the star. The birth radii are centered on center of the main galaxy in Au6. The different colour maps indicate in-situ or accreted particles, whereas the colour of the pixel indicates the number of stars.

3.4.1 In-Situ versus Accreted Stars

We now continue by looking at the difference between stars that are born in the galaxy, or born in a satellite and accreted at later times. For each galaxy, the fraction of in-situ over accreted stars for different metallicities is shown in Figure 19. This shows us that the exact fraction differs per galaxy, but for all of them the relative number of accreted stars increases as metallicity decreases. We see that Au6 by far has the lowest and Au16 the highest fraction of in-situ stars towards the low metallicity bins. Note, that the number of stars in the metal-rich bins is orders of magnitudes higher, so the overall fraction of in-situ stars will be determined by these metallicities.

Figure 20 shows the slopes for each metallicity bin for both the in-situ and accreted population. The in-situ population shows the same decrease in R with decreasing metallicity as in the previous section (i.e. Figure 16a), however we do not see this at all in the accreted population. For Au6, Au21 and Au23 R stays almost constant across all the metallicity bins, only decreasing a little bit. Au24 shows a different pattern, however, where its slope is a lot higher than the in-situ component in the metal-rich bin and is the highest amongst all the accreted populations. Its R also decreases a lot more than all of the other galaxies, following the same pattern as a lot of the in-situ populations. Finally, Au16 also decreases in R, but only in the extremely metal-poor bins. As the uncertainties are high for these metallicities, we cannot definitely say that this is an actual decrease in the rotation slope.

The velocity dispersions for the two components, shown in Figure 21, are less different from each other. Some galaxies have accreted populations that have overall higher $\sigma(v_{\rm gsr})$ than their in-situ counterparts, and for some this the exact opposite. The most striking difference is seen in Au16, where the accreted component has very high dispersions in the metal-rich bins and decreases significantly towards lower metallicities.

The complete mosaics of the $l - \overline{v}_{\rm gsr}$ and $l - \sigma(v_{\rm gsr})$ relations for all galaxies and bins separately can be found in Appendix A, Figures 30 and 31.

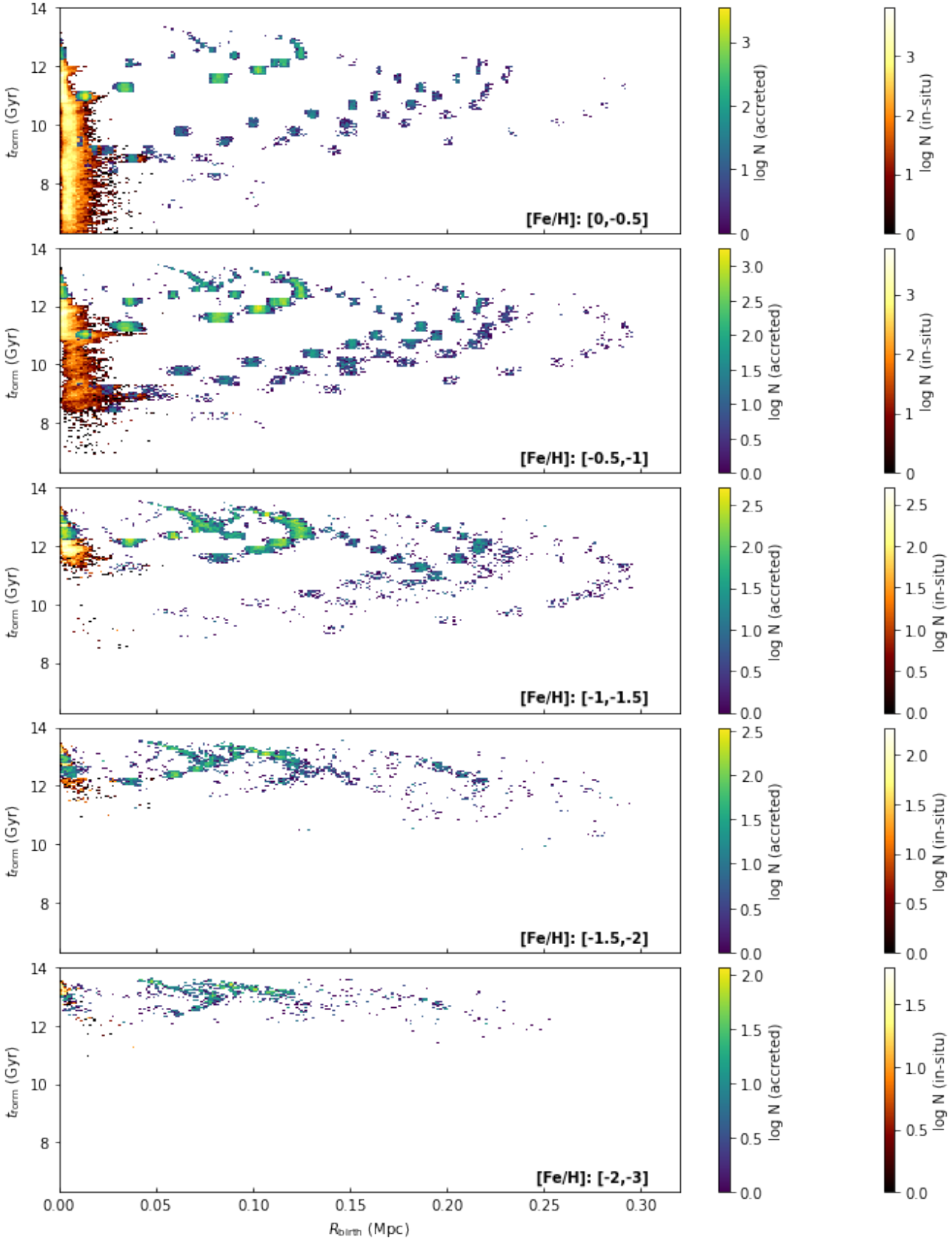

Figure 18: Similar to Figure 17, but the individual plots are split into specific metallicity intervals, displayed in the bottom right of the figure.

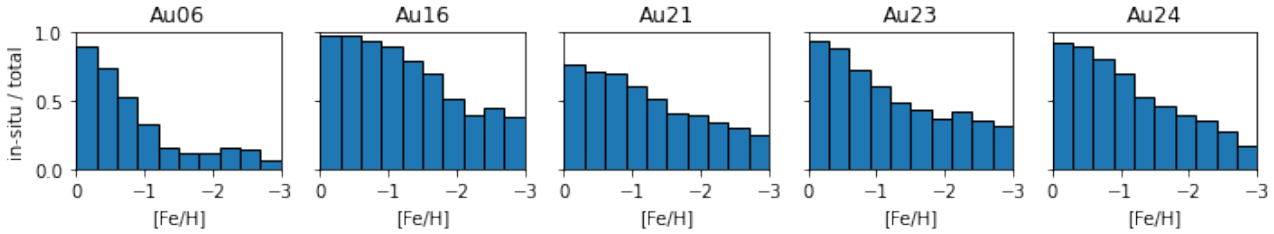

Figure 19: Fraction of the number of in-situ over the total number of stars in the metallicity bins of size 0.3dex for all halos. Note that the fractions are normalised separately in each bin, so the total fraction of in-situ stars is still dominated by metal-rich stars.

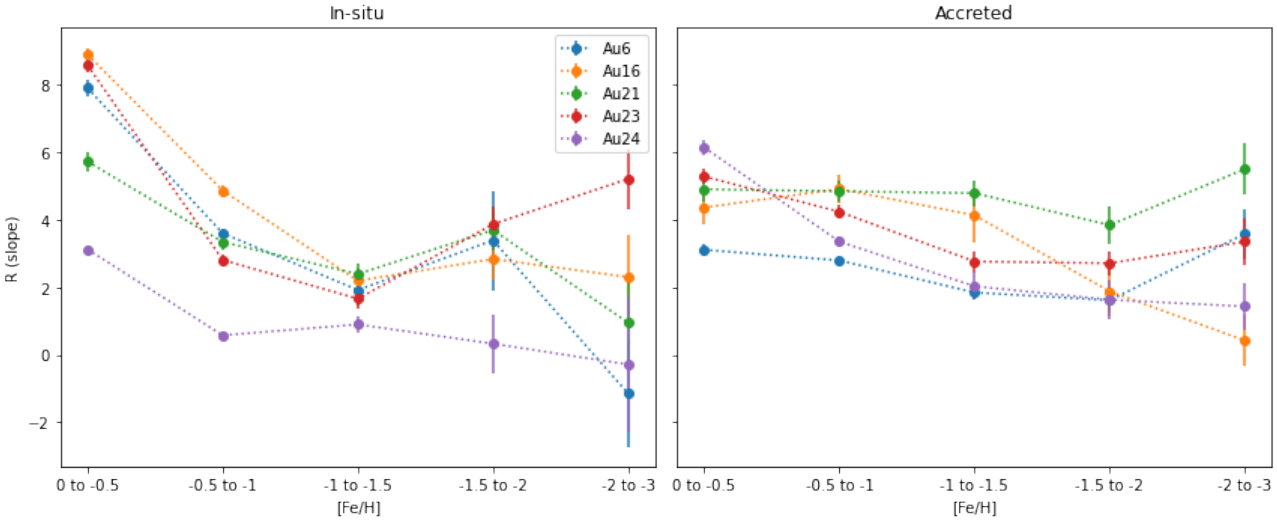

Figure 20: Similar to Figure 16a, but with the in-situ (left) and accreted (right) populations separated. The full mosaic can be found in Appendix A, Figure 30.

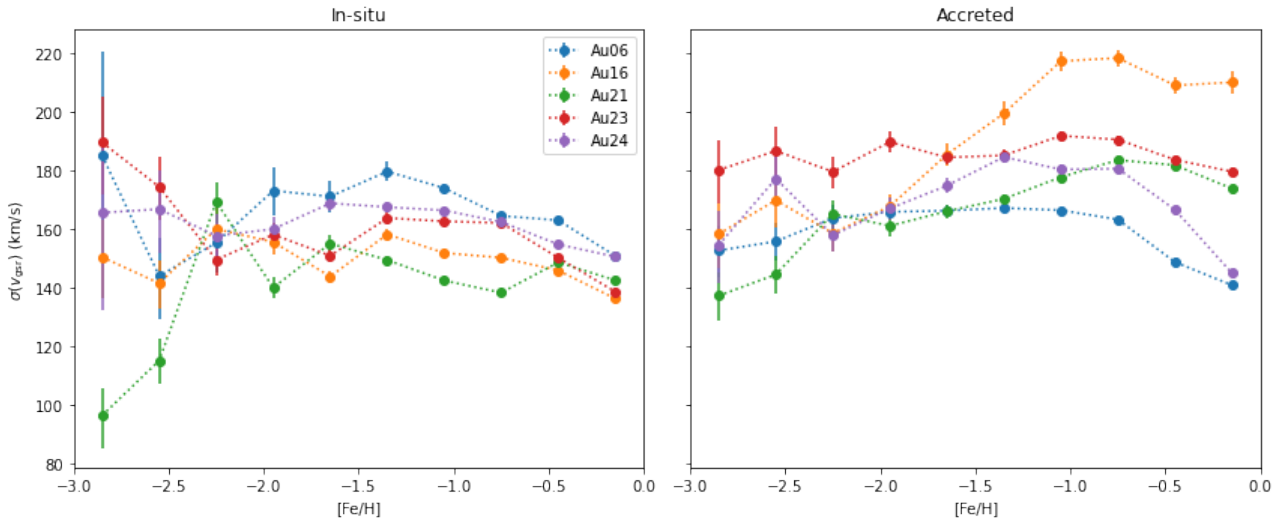

Figure 21: Similar to Figure 16b, but with the in-situ (left) and accreted (right) populations separated. The full mosaic can be found in Appendix A, Figure 31.

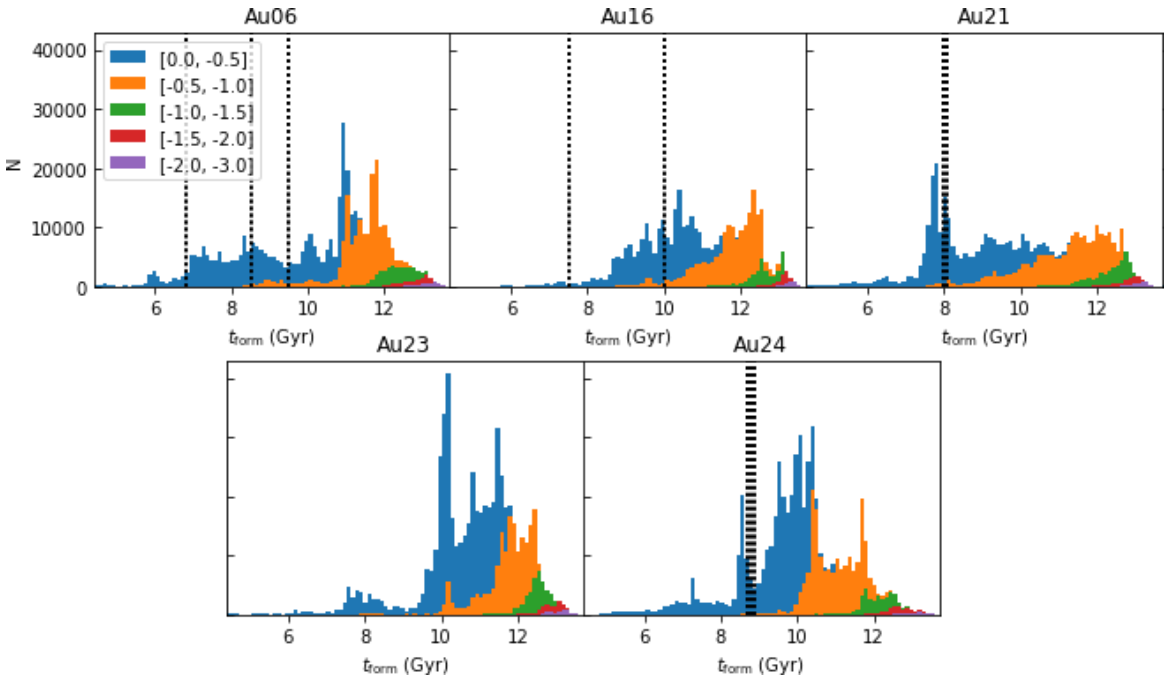

Figure 22: Histogram of ages for stars in the bulge of each Aurigaia halo. The different metallicity intervals have been separated into different colours. Times of major merger events for the halo are indicated by vertical black dashed lines. The approximate merger times are taken from Gargiulo et al. (2019), which only show them after $t_{\rm form} < 10\,{\rm Gyr}$ and for merger masses larger than $M_{\rm sat} > 10^{10}\,{\rm M}_{\odot}$. The thicker line (8 Gyr) in Au24 indicates two mergers, which are both a factor 10 more massive than the mergers in the other galaxies. The lines ($\sim 9\,{\rm Gyr}$) in Au24 indicates three mergers in close succession.

3.4.2 Age Dependence

Now, we focus on the actual age of the stars, which is expressed in Gyr. Figures 22 shows a histogram of the star ages for each galaxy, with the different metallicity bins colored differently. We notice that [Fe/H] indeed seems to be a good indication for age, but that it is not a perfect one-to-one relation as the overlap in the bins shows. We also note that the metallicity bins are not uniformly distributed over all ages, where our last three bins ([Fe/H] < -1) all have ages $t_{\rm age} \gtrsim 11$ and the first two span almost the entire range. In other words: the most metal poor stars in these simulations are exclusively old ($>12\,{\rm Gyr}$), but the more metal-rich populations show a wide range of ages. Since the mean age of stars each bin are still different, metallicity still gives a good indicator for young vs old stars, however if we want to have more detail in the range $8-11\,{\rm Gyr}$ we would need different bins.

In the same figure, some significant mergers are indicated with dotted vertical lines as well. These times have been taken from Figure 8 and 9 of Gargiulo et al. (2019), and are therefore approximate. Moreover, they only include mergers after 10 Gyr, with a total satellite mass greater than $10^{10}\,{\rm M}_{\odot}$. Most of the mergers in this figure are of this order, except from the two Au21 mergers around 8 Gyr, which both are in the order of $10^{11}\,{\rm M}_{\odot}$. With this information, we can see that Au21 and Au24 both have some very strong merger events after most stars in the [Fe/H] > -0.5 bins have already formed. The mergers in the other galaxies are more spread out, less frequent and/or less massive.

Figure 22, suggests that looking at the $l - \overline{v}_{\rm gsr}$ relation in age bins, can give us some more information about the pattern. We therefore choose an initial large bin of $[4, 8]\,{\rm Gyr}$, and then make bins with a width of 1 Gyr up to 14 Gyr. The fitted slopes in each of these bins can be seen in Figure 23. We now see that for Au6, Au16 and Au23 the decrease in R is a lot more gradual, which is likely due to the more evenly spaced bins. For the two galaxies with major mergers around $8-9\,{\rm Gyr}$ (Au21 and Au24) we see that R decreases a lot from the first to the second bin and then stays a lot more constant for all other times. This striking difference between the decrease in R in these galaxies suggests a possible connection to strong merger events. A hint for such a connection is also seen in other AURIGA galaxy bulges by Fragkoudi et al. (2020).

Some other connection seems to be that the galaxy with the fewest major mergers (Au23) seems to have the slowest decrease in R, followed by Au21 (2 mergers) and then Au6 (3 mergers). Finally, another interesting pattern in Figure 23 is that the R values for each of the galaxies seem to converge to a slope of $R \approx 3-4$ as we go to bins of higher star age.

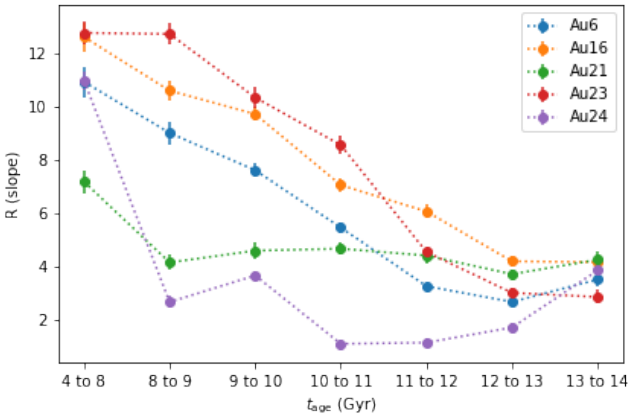

Figure 23: Similar to figure 16a, but with the stars binned by age (in Gyr, with $t = 0$ now), instead of metallicity ([Fe/H]).

4 Discussion and Future Work

After presenting our results, we will now dicuss our steps leading up to these results, and relate the results to the literature. We start by looking at some of the steps taken to create the mocks (Section 2.2), and by us in order to produce our results (Section 2.3).

4.1 Assumptions and Processing Steps

4.1.1 AURIGA and Aurigaia

In order to create the mock catalogues from AURIGA, the star particles from the simulation are expanded into individual stars, with similar kinematic properties to the original star particles. In our results we saw that the main effect of the additional stars was a perceived increase in sample size, and therefore lower uncertainties ($SE(\overline{v}_{\rm gsr}) \propto 1/\sqrt{N}$). The actual mean radial velocities did not seem to change significantly, so using the individual stars should not change our results. At the same time, the move from AURIGA to Aurigaia allows us to more precisely test our results by applying different observational selections.

Aurigaia additionally perturbes the stars' phase-space in order to avoid clumping behavior around the parent star particle. In applying this method, it is possible that the phase-space of the in-situ particles are smoothed out too much (see Section 2.2.5). Our results can be impacted by this by having overall flatter slopes (R) and velocity dispersions. In order to see if this phase-space smoothing has an actual effect, it would be possible to create similar plots by using the HITS-MOCKS, which do not use any phase-space smoothing.

Since we are using a simulation, the resolution is often going to be an important factor. The resolution used in Aurigaia was 'level 3' which corresponds to an average cell mass of $4 \times 10^4\,{\rm M}_\odot$ and $6 \times 10^3\,{\rm M}_\odot$ for dark and baryonic matter respectively (Grand et al., 2017). Originally a lower resolution (level 4) was used in AURIGA, of which the results of Gargiulo et al. (2019) and Blázquez-Calero et al. (2019) are based off. Even though Grand et al. (2017) concluded that re-running a halo did result in a similar galaxy across different resolution levels, there seems to be difference for Au24 and Au16. In the level 4 run, Au24 seems to form a bar which is clearly seen in the optical image, however in the re-simulated galaxy the bulge seems to be mostly spherical. For Au16 this is opposite, where the level 4 run seems to produce a spherical bulge and level 3 a clear bar. Both images for the galaxies can be seen in Figure 24. This shows that there is some difference between the re-simulations of the same halos, which means the categorisation of the bulges and merger data from Gargiulo et al. (2019) may be a little bit different for the Aurigaia galaxies.

4.1.2 Magnitude Cuts

In order to reduce the size of the mocks, all stars with $V > 16$ are removed (Section 2.2.6). One of the observational cuts by Arentsen et al. (2020a) is $13.5 < G < 16.5$, which would also include stars with $V > 16$ (very roughly: $V = 16 \implies G \approx 15.5$ for the red giants in this study). This implies that our sample size is lower, as we essentially have very little stars with magnitudes $G \gtrsim 15.5$. More importantly, the proportion of stars in the bulge with respect to fore-/background stars could change, which in turn could influence the

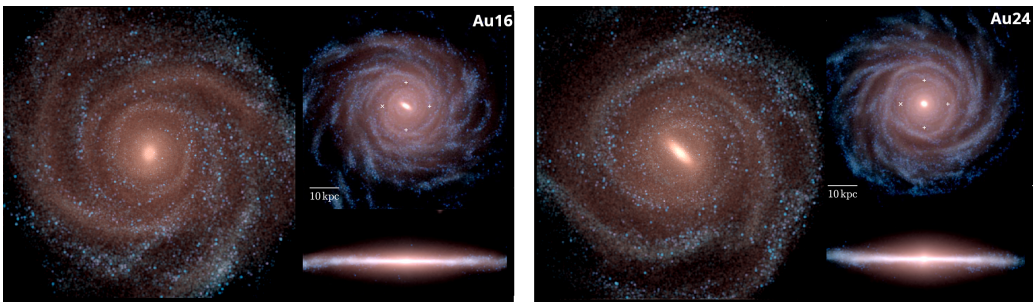

Figure 24: Crops from Figures 3 and 4, showing the difference between simulations at different resolution levels. For both Au16 and Au24, the respective left galaxy is run at the original resolution (level 4), and right is re-simulated with a higher resolution (level 3).

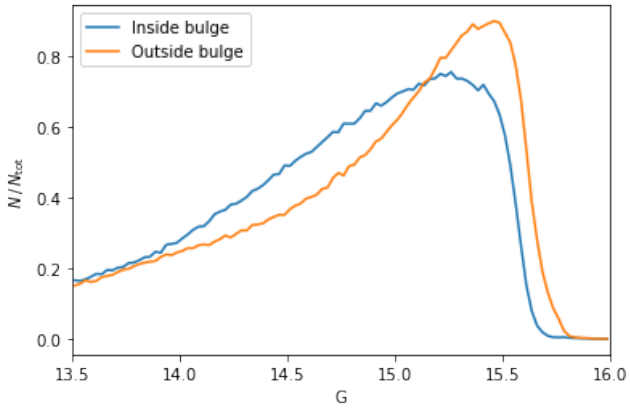

Figure 25: Normalized distributions of true G magnitudes for stars in- or outside the bulge (using cylindical selection with radius $R = 4\,\mathrm{kpc}$ and height $Z = 1\,\mathrm{kpc}$).

importance of selection effects. Figure 25 shows that the normalized magnitude distributions for stars inside and outside the bulge. The distribution of stars outside the bulks seems to peak towards a higher magnitude, than for stars inside the bulge. So it seems, assuming the distributions would continue similar to Figure 25, we would get more fore- and background stars if the $V > 16$ cut was not made by Aurigaia.

Continuing on magnitude cuts, we make the G cut on all our data when we create our own dataset to remove a lot of unnecessary stars. However, this could interfere with cuts that we make on uncertainty convoluted G values. Luckily, the impact of applying the observed G cut after the 'true' G cut is very minimal since the uncertainties are very low. For instance, in halo Au6 the observed G cut after the true G cut on all data only removes approximately 0.006% of the stars, which is negligible.

4.1.3 Metallicities

The metallicities ([Fe/H]) which we used for our results are not the original metallicities from the simulations (see Section 2.3.3). We derive them from a fitted $[Z]-[\mathrm{Fe/H}]$ relation based on actual [Fe/H] in Au6. Naturally, the best scenario would be to have snapshots for each of the halos, but as seen in figure 6, the relation between the two quantities seems very linear. The highest deviations from this relation, seem to occur at the lowest metallicities, where the number of stars is lowest as well. This spread in the $[Z]$ vs $[Z]-[\mathrm{Fe/H}]$ relation is higher than expected, and might be due to assumptions made by AURIGA. For instance, feedback mechanisms only return metals back into neighbouring gas cells, but not in nearby star particles. Since this physics of this regime are still relatively uncertain (Starkenburg et al., 2017a), we do not expect our linear fit to have a significantly lower physical meaning with respect to the simulated metallicities.

4.1.4 Assumed Bulge Sizes

Another discussion point is the bulge size we chose in order to select stars which are truly located into the bulge (Section 2.4.2). Here, we assume a cylindrical bulge with radius of 4 kpc and height of 1 kpc. However, Gargiulo et al. (2019) show that the sizes of the AURIGA bulges are different at $z = 0$ (radius of $\sim 4\,\mathrm{kpc}$ in Au6 and $\sim 2\,\mathrm{kpc}$ in Au24). To investigate whether the selected bulge size has any effect, we also added a selection

of bulge radius of 2 kpc for Au6 (similar to how we evaluate the other selection effects), but this did not show any significant differences in the mean radial velocities nor in the dispersions.

4.2 Comparison to Literature

The observations of Arentsen et al. (2020a) in the inner parts of the MW have shown that there is decrease in the dependence between mean radial velocity and galactic longitude as the stellar population decreases in metallicity. Moreover, the observations show a clear chemodynamical dependence in the velocity dispersions, where the dispersions increase with decreasing metallicity. The latter was also observed in RR Lyrae stars in the inner galaxy by Kunder et al. (2012). An analysis of the B/P bulges in AURIGA galaxies[15] by Fragkoudi et al. (2020) showed that for some of these bulges the $l - \overline{v}_{\rm gsr}$ relation flattened in the decreasing [Fe/H] bins: $[\mathrm{Fe/H}] > 0, [0, -0.5], [-0.5, -1], -1 > [\mathrm{Fe/H}]$. The decrease in rotation is different per galaxy and they showed that there seems to be a relation between the degree of flattening and the galaxies' merger history: galaxies with a recent and/or massive merger show a bigger fall-off in rotation in the [Fe/H] bins.

Our results combine those of Arentsen et al. (2020a) and Fragkoudi et al. (2020), by looking at the rotation patterns in AURIGA galaxies (similar to Fragkoudi et al., 2020) but also include the extremely metal-poor bins $[\mathrm{Fe/H}] : [-1.0, -1.5], [-1.5, -2.0]$ and $[-2.0, -3.0]$ (like Arentsen et al. (2020a)). Moreover, we investigate the effect of the observational cuts on this result. Our quantitative analysis showed that we see the same fall-off in rotation in the metal-poor bulge components of all the galaxies in our sample. The bulges in these galaxies have all been designated as PsBs, with only Au23 being a B/P bulge (Blázquez-Calero et al., 2019; Gargiulo et al., 2019). Therefore, we showed that the pattern occurs in multiple types of PsBs, not just in B/P bulges. Moreover, we quantitatively looked at the rotation in the in-situ and accreted bulge components, where we see that pattern in the in-situ population looks similar to the results of Arentsen et al. (2020a) and Fragkoudi et al. (2020), but the rotation in the accreted component stays more or less constant over all metallicities. This hints at a connection between the rotation fall-off and mergers, similar to what is suggested by Fragkoudi et al. (2020). To further explore this relation, and to see how good metallicity indicates age, we looked at the same rotational fall-off in star age-separated bins. We again see the same fall-off, but it is much more gradual. The fact that the pattern is much more gradual mostly comes from the fact that the metallicity bins span different star ages, whereas the star age specific bins are much more uniform. Notably, we see that the two galaxies with major mergers around 8 Gyr had a much more rapid fall-off in rotation than the other galaxies. It should be noted, that the latter result is qualitative and relies on the rough data given in Gargiulo et al. (2019). However, it still follows the merger-flattening relation as seen by Fragkoudi et al. (2020), and investigating this relation further with more precise merger data would be very interesting.

4.3 Lessons for the Milky Way

Besides looking at different types of galaxies and relating them to merger history, we have also looked at the roboustness of this pattern under observational effects. We strengthen the observations of Arentsen et al. (2020a) and possible future observations, by showing that the pattern remains essentially the same under a bunch of different observational effects, like field selection, foreground/background cuts and observational uncertainties. The main difference in the selections we made can be explained by the differing sample sizes that it resulted in. For the MW this means that the observations from Arentsen et al. (2020a) are representative for what is actually occuring, also at lower latitudes which are significantly more difficult to observe.

We have seen that the fall-off in rotation can be observed in a range of galaxies with different types of PsBs, including B/P bulges. This means that our MW is not unique in this regard and it should be visible in other PsBs galaxies as well.

There seems to be a relation between the rotational fall-off of metal-poor components and the merger history of the galaxy. In general, we see that galaxies that have had prominent mergers in relatively recent times, also show more flattening towards metal-poor populations. The results from Arentsen et al. (2020a) show that there still is quite some rotation in the MW bulge for metallicities $-1.5 < [\mathrm{Fe/H}] < -1.0$, which could then imply that the MW did not have a very prominent merger event at recent times. Hypothetically, it could be possible to quantify the relation between the rotation flattening in [Fe/H]-space and the time of the most recent merger. We could then observe the fall-off in the MW towards lower metallicities (like Arentsen et al., 2020a) and thereby put constraints on the merger history of the MW.

We also looked at the same rotation fall-off in age-space, where we saw that the difference between galaxies was even more pronounced than in [Fe/H] -space. Observing the stellar ages in the MW bulge would therefore give us a better indication of the rotational fall-off, and potentially allow us to put better constraints on the merger history of the MW. Unfortunately, the age of a star is quite difficult to determine in crowded areas, which is why we often use [Fe/H] as an indication of age.

[15] Au13, Au17, Au18, Au23 and Au26 identified as B/P bulges by Blázquez-Calero et al. (2019)

Future spectroscopic surveys can also help to get more and better data, such as the 4-metre Multi-Object Spectroscopic Telescope (4MOST) Disk & Bulge Survey at low resolution (Chiappini et al., 2019), which is able to push observations in the bulge towards the sub-giant branch. Together with metallicity data, it is then possible to derive ages of stars. In addition, this survey is able to use Pristine (Starkenburg et al., 2017b) data to find even more (very) metal-poor stars in the inner galaxy, increasing the sample size significantly. This survey can be complemented by surveys with the Multi-Object Optical and Near-infrared Spectrograph (MOONS) (Cirasuolo et al., 2020), which is able to take spectroscopic data in the near-infrared regime, and therefore provide this data for a lot more stars in heavily dust-obscured regions like the galactic plane.

5 Conclusion

In this thesis, we have seen that observations by Arentsen et al. (2020a) in the MW bulge show that stellar rotation in the plane of the galaxy decreases in lower metallicity populations. Moreover, this has also been observed in the cosmological MHD simulated galaxies (AURIGA, Grand et al., 2017) with B/P bulges by Fragkoudi et al. (2020). In addition, both see that the velocity dispersions in this region increases with decreasing metallicity.

By using the Gaia data release 2 mock of AURIGA (Aurigaia, Grand et al., 2018), we confirmed the results of Arentsen et al. (2020a) and Fragkoudi et al. (2020) in Aurigaia galaxies. In all of the galaxies with Pseudobulges we quantitatively showed that rotation is highest for the metal-rich population ($-0.5 < [\mathrm{Fe/H}] < 0$), decreases towards lower metallicities ($-1.0 < [\mathrm{Fe/H}] < -0.5$ and $-1.5 < [\mathrm{Fe/H}] < -1.0$) and finally stays roughly constant for the lowest metallicity populations ($-2.0 < [\mathrm{Fe/H}] < -1.5$ and $-3.0 < [\mathrm{Fe/H}] < -2.0$). However, we were unable to reproduce the observed velocity dispersions, since all of the dispersions in the Aurigaia galaxies were significantly higher than observed in the MW and also showed less increase towards lower metallicities.

In addition to reproducing rotation pattern using observational selections similar to Arentsen et al. (2020a), we were able to reproduce it using various selection strategies based on stellar parameters and observation fields, showing the roboustness of the pattern. This shows that the results of Arentsen et al. (2020a) are representative for actual kinematics in the MW, also at lower latitudes.

Throughout all this, we consider the rotations in [Fe/H]-space, and use it as an indicator for age. We also showed that this is a good approximation, in that the lowest metallicity stars are exclusively old ($> 12\,\mathrm{Gyr}$) and higher metallicity stars are mostly (but not all) younger. However there is significant spread in the metal-richer distributions and by separating populations by metallicity we lose a lot of information around ages $8 - 11\,\mathrm{Gyr}$. The rotational pattern in age-space, follows what we have seen before, but differences between galaxies are more pronounced. This shows the importance of deriving stellar ages, which might be possible in the MW with 4MOST (Chiappini et al., 2019).

By separating the in-situ and accreted populations and looking at their rotation patterns individually, we see that the in-situ population generally follows what we described before, but the accreted population shows almost constant rotation across all metallicities. Which hints at a connection with the merger events in the galaxy. To further investigate this connection, we use rough merger event data in these galaxies from Gargiulo et al. (2019). We qualitatively see that galaxies with major mergers less than $10\,\mathrm{Gyr}$ ago have a significantly earlier fall-off in rotation than galaxies with a more quiescent merger history. As this result relies on rough merger data, this has to be studied and quantified further, but shows potential for constraining the merger history of the MW.

6 Acknowledgements

I would like to thank Tom Callingham for helping out with accessing the Aurigaia data and providing wrapper code to load and process the dataset. His help came at precisely the right time, and resolved some crucial issues which allowed us to proceed with the analysis and finish the thesis.

I would also like to thank Anke Arentsen, who gave the starting point for the thesis with her results from PIGS, provided the data for the MW models used in the thesis and also gave some very helpful pointers towards crucial literature sources.

Finally, I would like to thank Else Starkenburg for being an amazing supervisor. She helped me at every step of the thesis, including understanding of the subjects involved, formulation and interpretation of the results and of course, by providing helpful feedback on all areas. Throughout the process I always felt free to ask questions and to engage in research myself. This thesis definitely would not have been possible without her!

For this thesis we have used data from Aurigaia, based on AURIGA. More information on this data and the project can be found on the Auriga Project website at http://auriga.h-its.org.

References

Arentsen A., et al., 2020a, Monthly Notices of the RAS, 491, L11

Arentsen A., et al., 2020b, Monthly Notices of the RAS, 496, 4964

Asplund M., Grevesse N., Sauval A. J., Scott P., 2009, Annual Review of Astronomy and Astrophysics, 47, 481

Babusiaux C., Gilmore G., 2005, Monthly Notices of the RAS, 358, 1309

Barbuy B., Chiappini C., Gerhard O., 2018, Annual Review of Astronomy and Astrophysics, 56, 223

Bensby, T. et al., 2017, A&A, 605, A89

Bland-Hawthorn J., Gerhard O., 2016, Annual Review of Astron and Astrophys, 54, 529

Bland-Hawthorn J., Krumholz M. R., Freeman K., 2010, The Astrophysical Journal, 713, 166

Blázquez-Calero G., et al., 2019, Monthly Notices of the Royal Astronomical Society, 491, 1800

Bradt H., 2004, Astronomy methods: A physical approach to astronomical observations. Cambridge University Press

Bruzual G., Charlot S., 2003, Monthly Notices of the Royal Astronomical Society, 344, 1000

Caffau E., Ludwig H. G., Steffen M., Freytag B., Bonifacio P., 2011, Solar Physics, 268, 255

Chabrier G., 2003, Publications of the Astronomical Society of the Pacific, 115, 763

Chambers K. C., et al., 2016, arXiv e-prints, p. arXiv:1612.05560

Chiappini C., et al., 2019, The Messenger, 175, 30

Cirasuolo M., et al., 2020, The Messenger, 180, 10

Clarkson W., et al., 2008, The Astrophysical Journal, 684, 1110

Diemand J., Madau P., Moore B., 2005, Monthly Notices of the RAS, 364, 367

Erwin P., et al., 2015, Monthly Notices of the RAS, 446, 4039

Fisher D. B., Drory N., 2016, An Observational Guide to Identifying Pseudobulges and Classical Bulges in Disc Galaxies. Springer International Publishing, Cham, pp 41–75, doi:10.1007/978-3-319-19378-6_3, https://doi.org/10.1007/978-3-319-19378-6_3

Fragkoudi F., et al., 2020, Monthly Notices of the RAS, 494, 5936

Gaia Collaboration et al., 2018, Astronomy and Astrophysics, 616, A1

Gallazzi A., Charlot S., Brinchmann J., White S. D., Tremonti C. A., 2005, Monthly Notices of the Royal Astronomical Society, 362, 41

Gargiulo I. D., et al., 2019, Monthly Notices of the Royal Astronomical Society, 489, 5742

Gennaro M., et al., 2014, in Formation and Evolution of the Galactic Bulge. p. 23

Grand R. J. J., et al., 2017, Monthly Notices of the RAS, 467, 179

Grand R. J. J., et al., 2018, Monthly Notices of the RAS, 481, 1726

Hunt J. A. S., Kawata D., 2014, Monthly Notices of the Royal Astronomical Society, 443, 2112

Hunt J. A. S., Kawata D., Grand R. J. J., Minchev I., Pasetto S., Cropper M., 2015, Monthly Notices of the Royal Astronomical Society, 450, 2132

Jenkins A., 2010, Monthly Notices of the RAS, 403, 1859

Kormendy J., Illingworth G., 1982, Astrophysical Journal, 256, 460

Kunder A. M., 2022, Universe, 8, 206

Kunder A., et al., 2012, Astronomical Journal, 143, 57

Kunder A., et al., 2016, Astrophysical Journal, Letters, 821, L25

Liu C., Bailer-Jones C. A. L., Sordo R., Vallenari A., Borrachero R., Luri X., Sartoretti P., 2012, Monthly Notices of the Royal Astronomical Society, 426, 2463

Lowing B., Wang W., Cooper A., Kennedy R., Helly J., Cole S., Frenk C., 2014, Monthly Notices of the Royal Astronomical Society, 446, 2274

Marinacci F., Pakmor R., Springel V., 2013, Monthly Notices of the Royal Astronomical Society, 437, 1750

Mateu C., Cooper A. P., Font A. S., Aguilar L., Frenk C., Cole S., Wang W., McCarthy I. G., 2017, Monthly Notices of the Royal Astronomical Society, 469, 721

McWilliam A., Zoccali M., 2010, The Astrophysical Journal, 724, 1491

Ness M., et al., 2013, Monthly Notices of the Royal Astronomical Society, 432, 2092

Planck Collaboration et al., 2014, Astronomy and Astrophysics, 571, A16

Planck Collaboration et al., 2016, Astronomy and Astrophysics, 594, A16

Rich R. M., Reitzel D. B., Howard C. D., Zhao H., 2007, The Astrophysical Journal, 658, L29

Romero-Gómez M., Figueras F., Antoja T., Abedi H., Aguilar L., 2014, Monthly Notices of the Royal Astronomical Society, 447, 218

Schaye J., et al., 2015, Monthly Notices of the Royal Astronomical Society, 446, 521

Schlegel D. J., Finkbeiner D. P., Davis M., 1998, The Astrophysical Journal, 500, 525

Schönrich R., Binney J., Dehnen W., 2010, Monthly Notices of the Royal Astronomical Society, 403, 1829

Shen J., Rich R. M., Kormendy J., Howard C. D., De Propris R., Kunder A., 2010, Astrophysical Journal, Letters, 720, L72

Sparke L. S., Gallagher III J. S., 2007, Galaxies in the universe: an introduction. Cambridge University Press

Springel V., 2010, Monthly Notices of the Royal Astronomical Society, 401, 791

Starkenburg E., Oman K. A., Navarro J. F., Crain R. A., Fattahi A., Frenk C. S., Sawala T., Schaye J., 2017a, Monthly Notices of the RAS, 465, 2212

Starkenburg E., et al., 2017b, Monthly Notices of the RAS, 471, 2587

Tumlinson J., 2010, Astrophysical Journal, 708, 1398

Vogelsberger M., Genel S., Sijacki D., Torrey P., Springel V., Hernquist L., 2013, Monthly Notices of the Royal Astronomical Society, 436, 3031

Wegg C., Gerhard O., 2013, Monthly Notices of the Royal Astronomical Society, 435, 1874

York D. G., et al., 2000, The Astronomical Journal, 120, 1579

Acronyms

4MOST 4-metre Multi-Object Spectroscopic Telescope

AGB asymptotic giant branch

AGN active galactic nuclei

B/P Boxy/Peanut

CFHT Canada-French-Hawaii Telescope

ClB Classical Bulge

CMD colour-magnitude diagram

Dec/δ declination

DR2 Gaia data release 2

GC galactic center

GSR galactic standard of rest

HB horizontal branch

IMF initial mass function

LSR local standard of rest

MHD magneto-hydrodynamical

MOONS Multi-Object Optical and Near-infrared Spectrograph

MW Milky Way

PIGS Pristine Inner Galactic Survey

PsB Pseudobulge

RA/α right ascension

RRL RR Lyrae star

SDSS Sloan Digital Sky Survey

SFR star formation rate

SNIa type Ia supernova

SNII type II supernova

SSP simple stellar population

A Figures

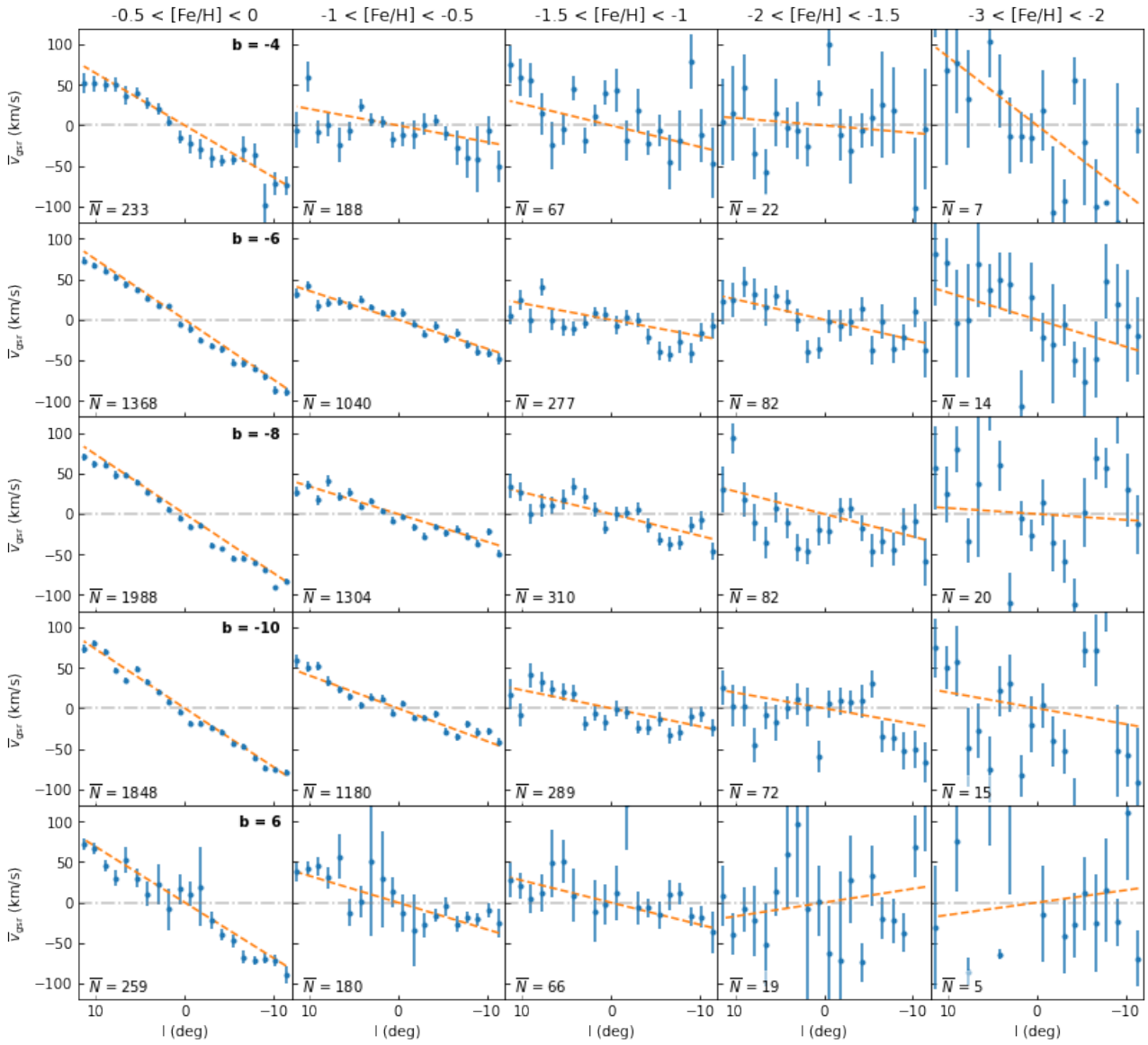

Figure 26: Similar to Figure 12, but for the latitude strip selections (selection 2) in Au6. A more compact view of the fitted slopes can be seen in Figure 15a.

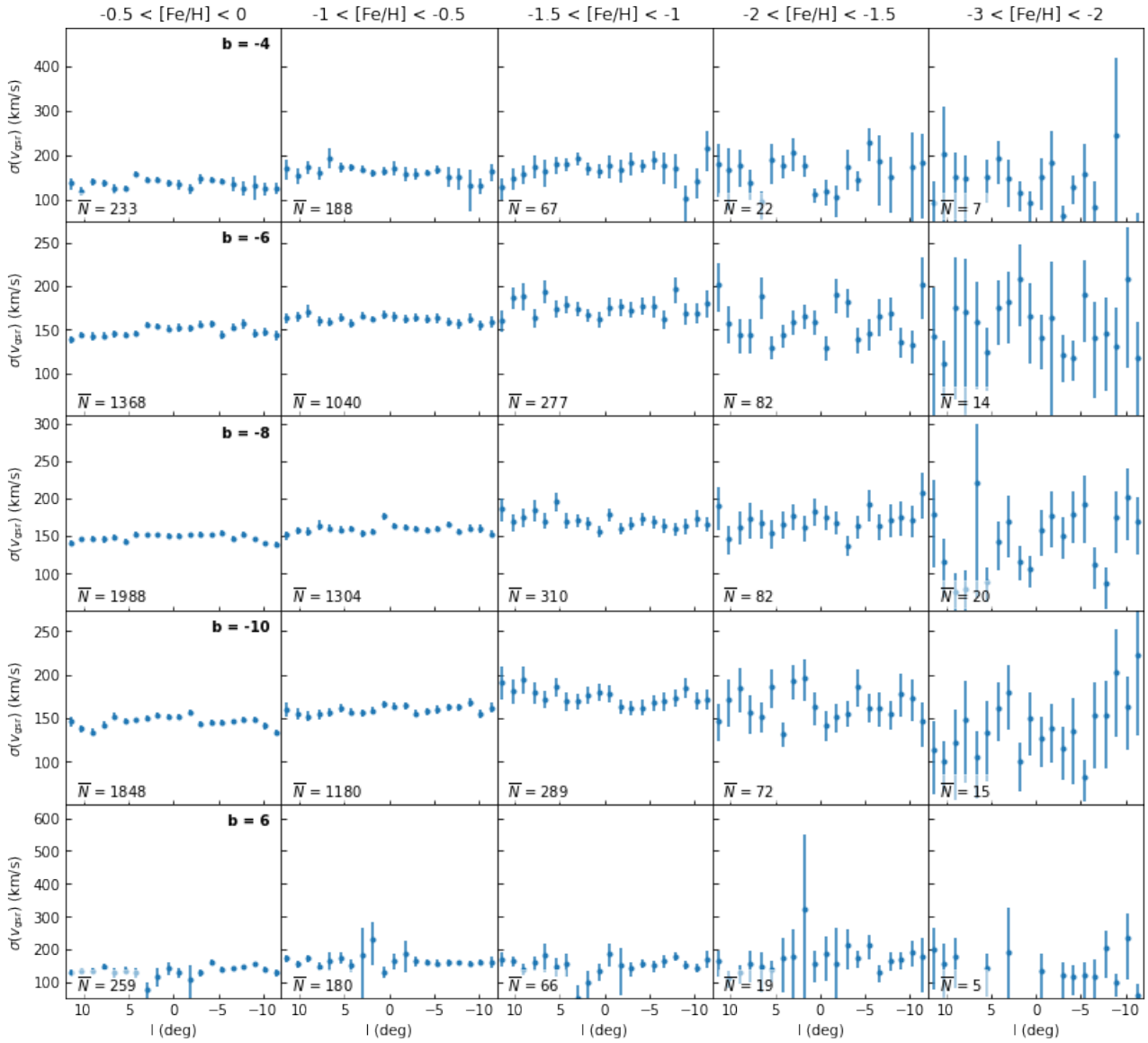

Figure 27: Similar to Figure 26, but for the velocity dispersions. A more compact view can be seen in Figure 16b.

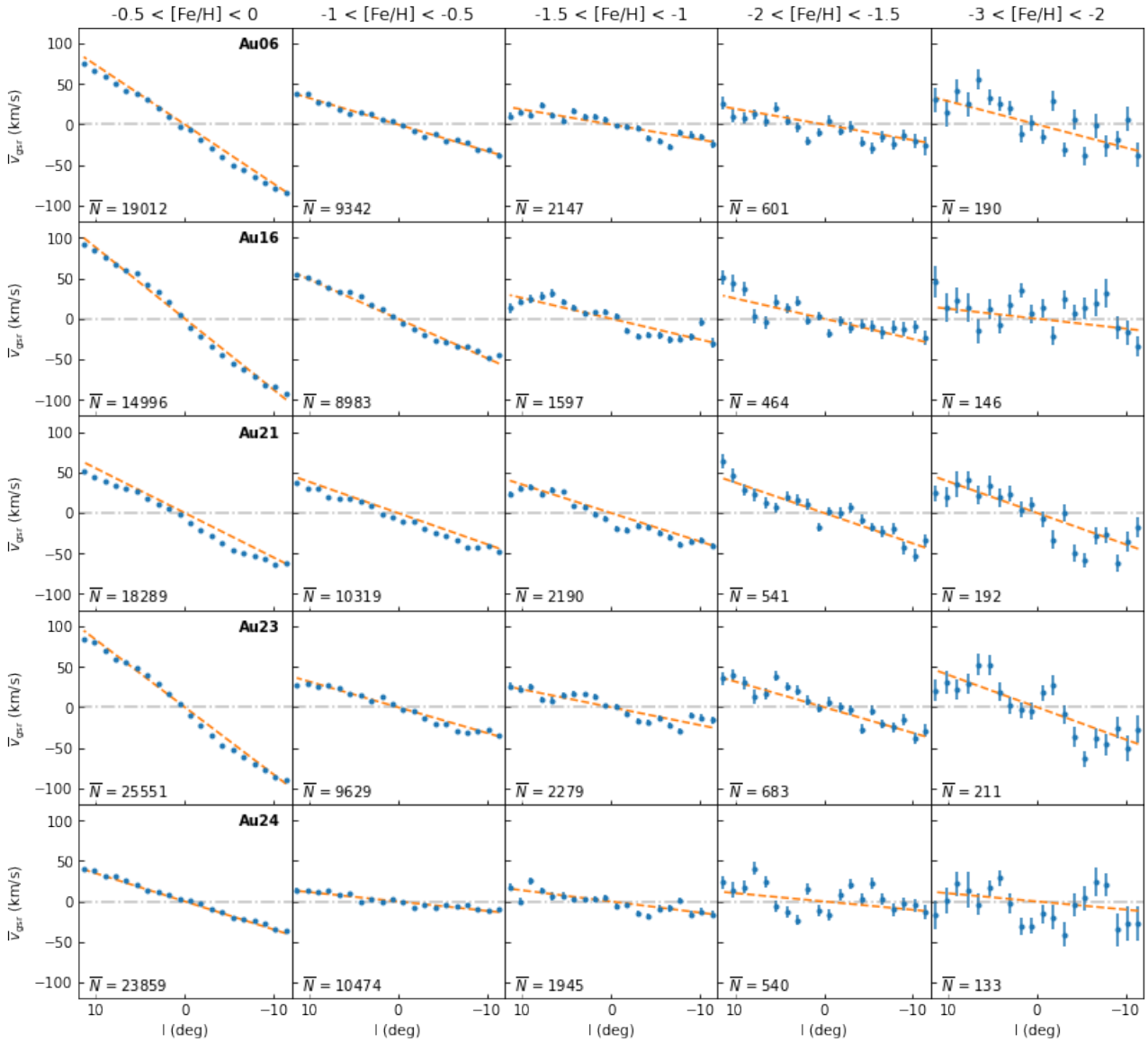

Figure 28: Similar to Figure 12, but for all halos. The selection used for all the halo uses the full box and stars with true positions in the bulge. A more compact view of the fitted slopes can be seen in Figure 16a.

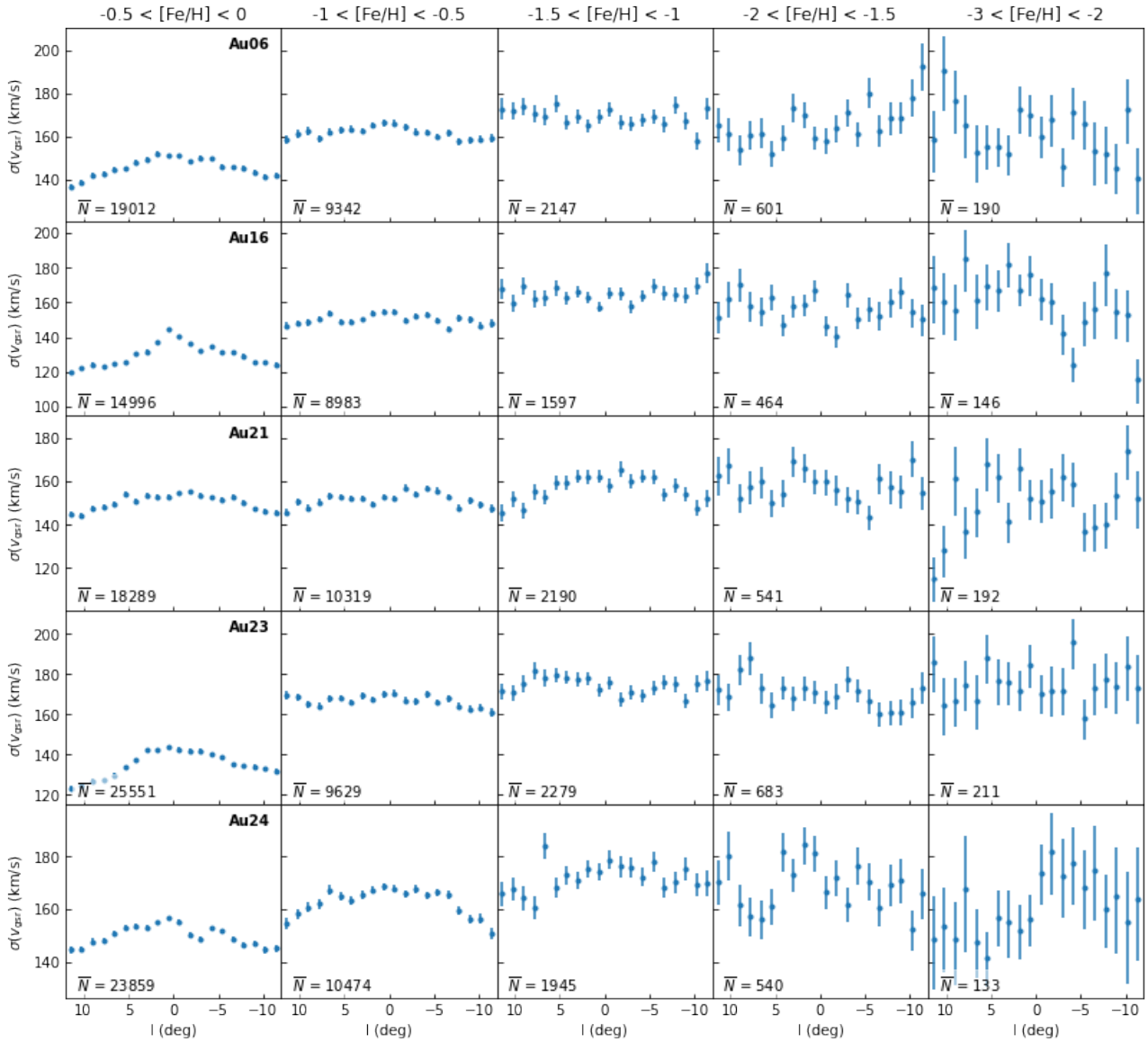

Figure 29: Similar to Figure 28, but for the velocity dispersions. A more compact view can be seen in Figure 16b.

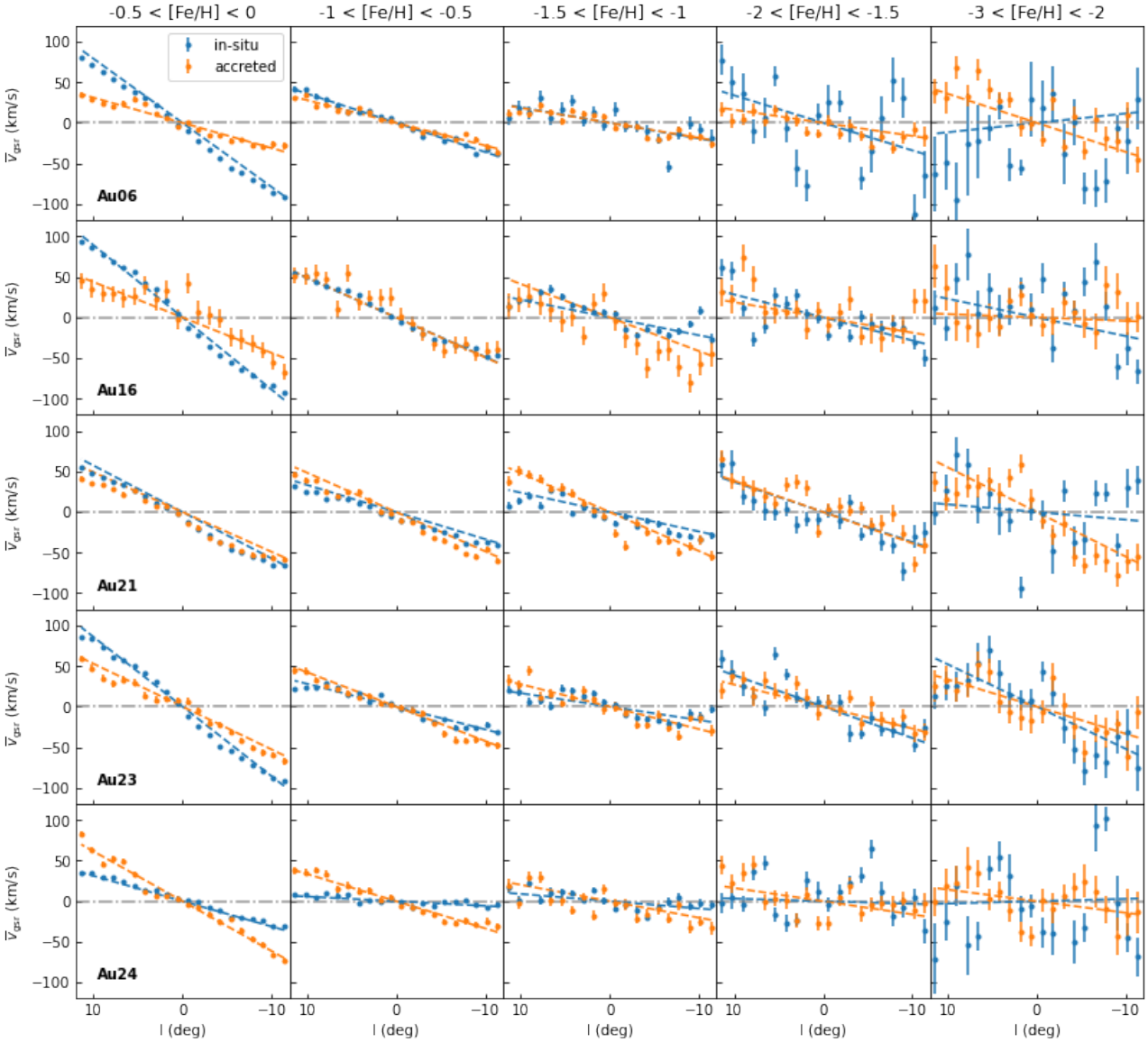

Figure 30: Similar to Figure 28, but with the in-situ and accreted populations separated. A more compact view of the fitted slopes can be seen in Figure 20.

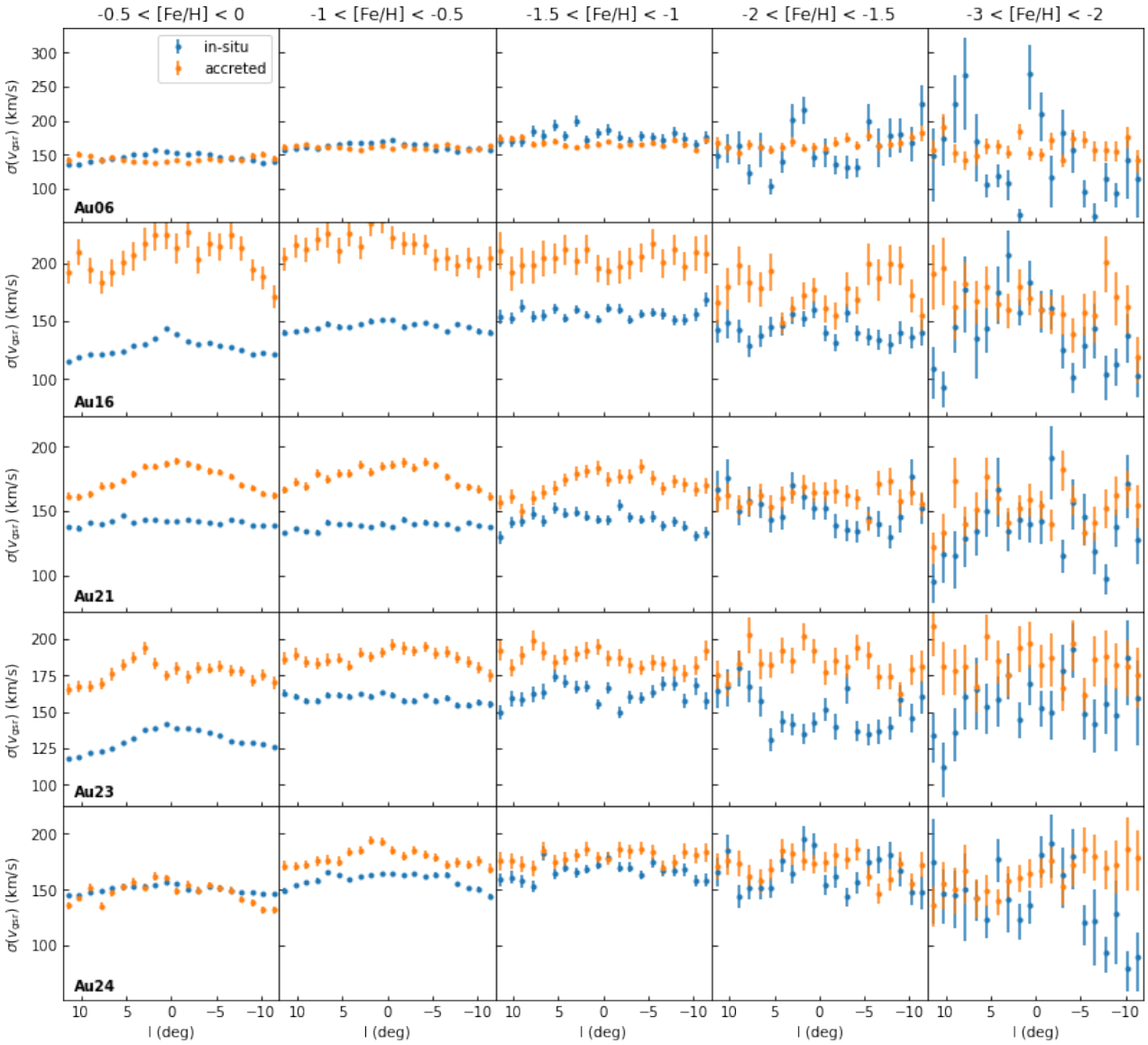

Figure 31: Similar to Figure 28, but with the in-situ and accreted populations separated. A more compact view of the fitted slopes can be seen in Figure 21.

B Tables

l (deg)	b (deg)	l (deg)	b (deg)
-8.3400	10.2810	5.2928	-6.6449
-2.6747	8.5868	6.7759	-7.2137
7.4013	-8.2669	2.4711	-5.1224
-3.0430	10.6548	5.3122	-4.0879
-6.7530	8.7938	6.6103	-10.8908
-5.3007	10.3496	3.3348	-3.3600
-3.6258	5.3524	1.4733	-3.7986
5.6931	-8.4823	3.5425	-7.5296
10.0365	-10.0418	4.8560	-4.8393
8.6119	-10.0540	7.1027	-5.2878
5.3369	-9.9443		

Table 1: Galactic coordinates for the centers of the observation fields used in the PIGS observations (Arentsen et al., 2020a)

Halo	$V_{\rm LSR}$ (km s^{-1})
Au06	229.2226
Au16	213.5378
Au21	226.5683
Au23	234.6172
Au24	218.7874
MW	238 ± 15

Table 2: Local standard of rest values for each halo, in the Y direction. These values are computed by spherically averaging the stars around the solar position. The MW value is taken from Bland-Hawthorn & Gerhard (2016).

Halo	$\frac{M_{vir}}{10^{12}\,{\rm M}_\odot}$	$\frac{R_{vir}}{\rm kpc}$	$\frac{M_\star}{10^{10}\,{\rm M}_\odot}$	$\frac{M_{\star,d}}{10^{10}\,{\rm M}_\odot}$	$\frac{R_d}{\rm kpc}$	$\frac{V_c\,(R_\odot)}{\rm km\,s^{-1}}$	$\frac{\Sigma\,(R_\odot)}{\rm M_\odot/pc^2}$	$\frac{h_z\,(R_\odot)}{\rm pc}$	$\frac{\sigma_z\,(R_\odot)}{\rm km\,s^{-1}}$
Au 06	1.01	211.8	6.1	2.6	3.3	224.7	33.2	339 (1139)	39.8
Au 16	1.50	241.5	7.9	3.7	6.0	217.5	44.5	303 (1130)	40.2
Au 21	1.42	236.7	8.2	3.8	3.3	231.7	51.8	430 (1363)	44.0
Au 23	1.50	241.5	8.3	4.0	5.3	240.0	52.5	339 (1260)	42.0
Au 24	1.47	239.6	7.8	2.8	6.1	219.2	31.5	330 (1436)	42.4
MW	1.3 ± 0.3	†220.7	6 ± 1	4 ± 1	2.6 ± 0.5	238 ± 15	33.3 ± 3	‡300 ± 50 (900 ± 180)	‡25 ± 5 (50 ± 5)

Table 3: Table of properties of each simulation. Both the table and this caption are directly taken from Grand et al. (2018), with Au27 omitted. The columns are (1) halo number, (2) virial mass, (3) virial radius, (4) stellar mass within the virial radius, (5) stellar disc mass calculated as $2\pi\Sigma_0 R_d^2$, where Σ_0 and R_d are the parameters retrieved from a bulge-disc surface density decomposition performed in the same way as in Grand et al. (2017) for the mass within 1 kpc of the disc mid-plane, (6) stellar disc scale length, (7) circular rotation velocity at a radius of 8 kpc, calculated as $V_c = \sqrt{GM(< R = 8\,{\rm kpc})/8\,{\rm kpc}}$, (8) azimuthally averaged stellar surface density within 1 kpc of the mid-plane at $R = 8$ kpc, (9) thin and thick (bracketed values) disc scale heights of a double sech2 decomposition of the vertical density distribution in a 1 kpc-wide annulus centred at $R = 8$ kpc and (10) vertical velocity dispersion of stars within 1 kpc of the disc mid-plane at $R = 8$ kpc. The last row provides current estimates of all of these quantities for the Milky Way. All values are taken directly from Bland-Hawthorn & Gerhard (2016). †The mean of values for R_{200} provided in table 8 of that paper, the standard deviation of which is 28.6. ‡Observationally derived vertical scale height and velocity dispersion of the old thin disc and thick disc (bracketed values) at the solar neighbourhood

C Code

The code used to produce the results for this thesis can be found in the following Github repository: https://github.com/StenSipma/Astronomy_Bachelor_Thesis. Note that this code is written in Jupyter notebooks, and is not necessarily written with other users in mind. However, we still share it for transparency and also in the hope that pieces of the code will still be useful for other users.